Nonlinear Dynamic Analyses of Austrian Dam in the 1989 Loma Prieta Earthquake

By

Ross W. Boulanger, PhD, PE, F.ASCE
Professor, Department of Civil and Environmental Engineering,
University of California at Davis, Davis, CA 95616
E-mail: rwboulanger@ucdavis.edu

JGGE – Accepted May 2019

ABSTRACT

Two-dimensional nonlinear dynamic analyses (NDAs) of Austrian Dam in the 1989 M_w=6.9 Loma Prieta Earthquake are presented using the finite difference program FLAC 8.0 with the user-defined constitutive model PM4Silt and following engineering procedures common in practice. This relatively homogenous, 55-m high embankment dam was comprised primarily of low-plasticity clayey sands and clayey gravels. The dam experienced estimated peak ground accelerations of 0.4-0.6g during the earthquake and developed extensive cracking with crest settlements up to 859 mm. The engineering properties of the compacted embankment materials are estimated based on the available isotropically consolidated undrained triaxial compression and resonant column test data. NDAs were performed using two alternative calibrations for the PM4Silt model and four different input motions. Sensitivity of the computed deformations to various modeling parameters and assumptions was examined. The computed responses are shown to be in reasonable agreement with the observed crest settlements, embankment deformation patterns, and excess pore pressures. Limitations in the material characterizations and analysis procedures and their possible effects on the analysis results are discussed. The results of this study provide support for the use of these analysis methods and engineering procedures in seismic evaluations of compacted earthfill embankments.

INTRODUCTION

Austrian Dam, a 55-m-high compacted earth embankment dam located in Santa Clara County in California, experienced significant damage during the 1989 M_w=6.9 Loma Prieta Earthquake. The embankment was to have an upstream impervious zone and a downstream pervious zone based on selective borrowing, but was homogenous for practical purposes with both zones comprised primarily of low-plasticity clayey sands and clayey gravels. Peak horizontal ground accelerations at the dam site are estimated to have been between 0.4 and 0.6 g. The dam experienced crest settlements of 750 to 859 mm along 140 m of its approximately 230-m-long crest. Extensive cracking in the embankment required removal and replacement of the upper portion of the embankment, and extensive damage to the spillway led to eventual construction of a new spillway. Details of the dam's characteristics and its performance in

the Loma Prieta Earthquake are provided by Wahler Associates (1979, 1981, 1990), Babbitt (1991), and Harder et al. (1998).

Options for constitutive modeling of compacted clayey fills or clays in nonlinear dynamic analyses (NDAs) are limited in practice, such that it is common for clay-like soils to be represented in an NDA using total stress (e.g., Mohr Coulomb) or total stress hysteretic models that do not simulate key features of cyclic softening, pore pressure generation, or shear strain accumulation (e.g., Rampello et al. 2009, Stark et al. 2012, Hadidi et al. 2014, Luque and Bray 2017). For example, the only published NDA for Austrian Dam used a Mohr Coulomb based model (Vrymoed and Lam 2006). Advanced constitutive models for clays have been used in seismic analyses of embankment dams (e.g., Mejia et al. 1992, Elia and Rouainia 2013), but there remains a need for further development, implementation, and validation of these types of models in the analysis programs most commonly used in practice. The constitutive model PM4Silt (Boulanger and Ziotopoulou 2018) was recently developed for representing clays and plastic silts in NDAs using FLAC 8.0 (Itasca 2016), and provides an opportunity to reevaluate the Austrian Dam case history using a more advanced constitutive model.

This paper presents results of two-dimensional (2D) NDAs of Austrian Dam in the 1989 M_w=6.9 Loma Prieta Earthquake using the finite difference program FLAC 8.0 (Itasca 2016) with the user-defined constitutive model PM4Silt (Boulanger and Ziotopoulou 2018) and following engineering procedures common in practice. The characteristics of the dam and its performance in the Loma Prieta Earthquake are summarized. The engineering properties of the compacted embankment materials are re-evaluated and two alternative calibrations for the PM4Silt model are developed. Analyses to establish the initial static stress and seepage conditions are described. NDAs are then presented for the two alternative PM4Silt model calibrations and four different input motions. Sensitivity of the computed deformations to various modeling parameters and assumptions is examined. The computed responses are shown to be in reasonable agreement with the observed crest settlements, embankment deformation patterns, and excess pore pressures. Limitations in the material characterizations and analysis procedures and their possible effects on the analysis results are discussed. The results of this study are shown to provide support for the

use of these analysis methods and engineering procedures is seismic evaluations of compacted earthfill embankments.

AUSTRIAN DAM AND ITS PERFORMANCE IN THE LOMA PRIETA EARTHQUAKE

Austrian Dam is a 55-m-high compacted earthfill embankment dam located on the upper portion of Los Gatos Creek in Santa Clara County. The dam, completed in 1951, retains a reservoir (Lake Elsman) with a capacity of 7.7 million m^3 and freeboard of 4.6 m. A plan view and cross-section of the maximum section (A-A') are shown in Figures 1 and 2, respectively. The dam crest is at elevation 342.9 m and has a width of 6.1 m and length of about 230 m. The upstream and downstream slopes range from 1.5:1 (horizontal to vertical) near the crest to 3.5:1 near the toes. Construction drawings indicate that the dam was to have upstream impervious and downstream pervious zones based on selective borrowing, but the as-constructed embankment is nearly homogenous for practical purposes. The dam is founded on the Franciscan Formation, including sandstones, siltstones, shales, and greywacke. The central portion of the downstream shell was to be underlain by seven gravel strip drains spaced 9.3-m apart over the bedrock. The drains were absent in one of four trenches excavated near the downstream toe in 1989, suggesting the drains may not all have been constructed as specified (Babbitt 1991). Additional details of the dam construction, material properties, and performance in the Loma Prieta Earthquake are provided in Wahler Associates (1979, 1981, 1990), internal memos on public file at the California Division of Safety of Dams (e.g., Babbitt 1991), and Harder et al. (1998).

The embankment materials were comprised primarily of low-plasticity clayey sands (SC) and clayey gravels (GC) with fines contents (passing No. 200 sieve) ranging from 16-44% (mean of 32%) and gravel contents (coarser than No. 4 sieve) ranging from 26-72% (mean of 46%). The matrix materials had plasticity indices (PI) ranging from 11-15 (mean of 13). The mean dry unit weight of the as-compacted materials during construction was about 19.0 kN/m^3 versus about 19.9 kN/m^3 for samples obtained from borings in 1989. Babbitt (1991) reviewed original construction records, settlement data, repair records, and supporting laboratory test data, and concluded that the average as-compacted unit weight,

corresponding to about 93% of the DWR 20,000 ft·lb/ft^3 compaction standard, was reasonable for the general embankment. Classification and compaction test data are summarized in Table 1.

The dam is located over the up-dip edge of the Loma Prieta fault plane projection by Wald et al. (1991) as shown in Figure 3. The nearest strong motion recordings were at the Corralitos station, which is also located over the up-dip edge of the fault plane projection at a similar epicentral distance as Austrian Dam. The next nearest strong motion station was at Lenihan Dam, which is located at slightly greater distances from the epicenter and fault plane than is Austrian Dam. The Corralitos station is on predominantly shale landslide deposits that have a measured V_{s30} (i.e., average shear wave velocity to a depth of 30 m) of 462 m/s (Gibbs et al. 1992), whereas the Lenihan abutment station is on Franciscan formation rocks with an inferred V_{s30} of 1,070 m/s (CESMD 2019) consistent with geophysical measurements summarized in Makdisi et al. (1991). There does not appear to be any record of geophysical measurements at Austrian Dam, but unpublished data from a limited number of other projects in the region have shown shear wave velocities ranging from 760 to 2,700 m/s in the upper 30 m of the Franciscan formation. Channel 1 at the Corralitos and Lenihan stations is oriented due east, which is approximately transverse to Austrian Dam. The recorded horizontal acceleration time series and corresponding acceleration response spectra for the Corralitos station and the abutment station at Lenihan Dam are shown in Figure 4. The Corralitos motions had slightly greater peak accelerations (0.48-0.63 g) than the Lenihan abutment motions (0.41-0.44 g), but lower spectral accelerations for periods greater than about 0.8 s. The longer-period components of the Lenihan abutment motions may have been influenced by the dynamic response of the dam, but the extent of such interaction is uncertain. The motions at the Austrian Dam site were not recorded, but it seems reasonable to expect that they would have had similar characteristics to those recorded at the Corralitos and Lenihan abutment stations based on the relative proximities to the fault plane projection and earthquake epicenter.

The reservoir and phreatic levels in the dam were low at the time of the earthquake, as shown on Figure 2. The reservoir was about 30 m below the dam crest and had been similarly low for three or four years prior to the earthquake because of drought conditions. Piezometric levels were monitored by pairs

of standpipe piezometers placed in three boreholes at the locations shown on Figure 1 and to the depths shown on Figure 2. The piezometer pairs in each borehole had 5-foot sensing intervals (sand packing) separated from each other by bentonite pellets (Vrymoed and Lam 2006). The piezometers were recorded on October 16, 1989, only one day before the earthquake; the piezometric levels and inferred phreatic surface from these recordings are shown on the cross-section in Figure 2. Piezometers P-3 and P-5 were dry. The piezometers were recorded again on October 19, 1989, only 2 days after the earthquake. The post-earthquake piezometer readings showed rises of 2.7 m to 16.8 m, as discussed later with the numerical simulation results. The post-earthquake recordings showed that the excess pore pressures dissipated relatively slowly; e.g., the excess heads of 15.2 m and 16.8 m measured in piezometers P-6 and P-1 two days after the earthquake, dropped about 7.5 m (about 50% of 15.2 m) and 1.3 m (about 8% of 16.8 m) over the next 10 days (Wahler Associates 1990, Vrymoed and Lam 2006). The observed slow rates of dissipation suggest that excess heads immediately after the earthquake may have been 0-10% greater than the values measured two days after the earthquake and that essentially undrained loading conditions existed during earthquake loading. These piezometer data provide a basis for calibrating the seepage analyses, as well as evaluating model predictions of excess pore pressure after strong shaking.

The embankment experienced extensive cracking and deformation during the earthquake. The areas of significant longitudinal and transverse/oblique cracking were mapped as shown on Figure 1. The photograph in Figure 5a shows the cracking along the dam crest near the left abutment, whereas the photograph in Figure 5b shows the cracking and distortion along the access road on the downstream face of the dam. At the left abutment, transverse cracks in the embankment were up to 200 mm wide and up to 3 m deep, and cracks along the embankment-foundation contact were up to 450 mm wide and up to 8 m deep (Harder et al. 1998). The cracking along the embankment-foundation contact was associated with loose fill or slope debris materials that appear to have not been removed from the abutment slope during construction (Wahler Associates 1990). At the right abutment, cracks and separations at the contact between the embankment and the spillway walls were up to 250 mm wide and up to 7 m deep (Harder et al. 1998). Longitudinal cracks in the upper portions of the upstream and downstream faces were up to 100

mm wide shortly after the earthquake, but widened to as much as 300 mm at the surface over the following couple of weeks. Trenches showed the cracks extending to depths of about 4.3 m with widths that tapered with depth. The progressive widening of the longitudinal cracks with time was generally attributed to soil creep during this period. Limited longitudinal cracking and minor bulging was also observed on the downstream face near the toe. In addition, the tubing for piezometer P-1 (located midway down the downstream face) was observed to be deformed between elevations 291.1 m and 292.6 m (or about 7.6 to 9.1 m above the bedrock), and the tubing for piezometer P-6 (located at the dam crest) was deformed between elevations 310.2 and 317.2 m (about mid-height in the embankment).

Survey monuments along the dam crest were surveyed on October 16, 1987, one day before the earthquake, and then again on October 18, one day after the earthquake. The survey measurements showed that the dam crest settled 750 to 859 mm over the central 140 m of the crest length. Horizontal displacements along the dam crest were more varied, with the measurements indicating a maximum of 330 mm in the downstream direction near the right abutment and a maximum of 130 mm in the upstream direction closer to the left abutment. Harder et al. (1998) noted the surveys were not tied into a stationary benchmark, and concluded instead that the right side of the embankment likely moved about 460 mm downstream relative to the left abutment. Survey measurements over the following 19 days did not show any measurable increase in displacements with time (Vrymoed and Lam 2006).

The embankment damage was repaired within two months of the earthquake and a new spillway was constructed on the left abutment in 1993-94. The embankment repairs included excavating and replacing fills in the areas of observed cracking, the addition of blanket and chimney drains at both embankment ends, grouting of the embankment-foundation contact at the left abutment, epoxy grouting of the cracks in the spillway, and grouting of voids beneath the spillway slabs (Harder et al. 1998).

MATERIAL PROPERTIES AND CONSTITUTIVE MODEL CALIBRATION

The cross-sections and internal zoning used for the 2D nonlinear dynamic analyses are shown in Figure 6. The upstream pervious, downstream impervious, and gravel strip drain zones are assigned different hydraulic conductivities, but are all modeled using the same set of mechanical properties with

the constitutive model PM4Silt. The same mechanical properties are assigned to the upstream and downstream zones because field investigations showed them to be largely indistinguishable in gradations and engineering properties (Figure 7). The composite strength of the gravel strip zone may be greater than that of the material between the strips alone, but neglecting the strengthening effect of the gravel strips in this zone would be a conservative approximation and would not be expected to significantly affect the response of the overall structure. The bedrock was modeled as a rigid base for the mesh shown in Figure 6a, which also may be slightly conservative but is a reasonable simplification given the absence of shear wave velocity data for the bedrock and the uncertainty in the input ground motions. The second mesh shown in Figure 6b uses the same embankment mesh as Figure 6a, but includes a 60-m-thick layer of bedrock with a compliant base and free-field lateral boundary conditions (Itasca 2016); this mesh will be used later to evaluate sensitivity of the computed responses to a range of possible bedrock shear wave velocities. The remainder of this section focuses on the calibration of the PM4Silt model for the compacted fills, whereas details of the analyses for initial static stresses and dynamic response are covered in the following sections.

The PM4Silt model was chosen for representing the compacted fills because their engineering properties appear to be largely governed by the clayey matrix materials (i.e., fines content of 16-44%, PIs of 11-15) and thus better modeled as clay-like than sand-like. The PM4Silt model builds on the framework of the stress-ratio controlled, critical state compatible, bounding surface plasticity PM4Sand model (Ziotopoulou and Boulanger 2016) with modifications to better approximate the monotonic and cyclic undrained loading responses of clays and plastic silts. Calibration procedures for PM4Silt with different types of available information are illustrated in Boulanger et al. (2018), and so are only briefly described herein. The calibration process involved: (1) establishing relationships for undrained shear strength (s_u) and small-strain shear modulus (G_{max}) as functions of the consolidation stress conditions, (2) adjusting the parameter h_o to obtain reasonable results for shear modulus reduction and equivalent damping ratio versus shear strain amplitude, (3) adjusting the parameter h_{po} to obtain reasonable cyclic strength curves, (4) adjusting other secondary parameters to obtain reasonable rates of shear strain

accumulation at larger strains, and (5) iteratively repeating the above steps until no further adjustments are warranted. Two alternative calibrations were developed, with all parameters listed in Table 2. The following discussion elaborates on the calibration steps, the differences in the two calibrations, and the calibrated model responses.

Monotonic undrained shear strength parameters were obtained from the isotropically consolidated, undrained (ICU) triaxial compression test data for tube samples by Wahler Associates (1981), reinterpreted using the approach in Duncan and Wright (2005). Test specimens were reconsolidated in the laboratory to isotropic effective stresses that are in the range of the vertical or mean effective stresses that existed at the sampling depths. Strength parameters were developed for two different failure criterion: (a) peak effective stress ratio or stress obliquity, which occurred at axial strains of about 3-6%, or (b) an axial strain of 10%. The test specimens had strain-hardening responses (incrementally dilative in monotonic shearing at larger strains), as shown in Figure 8, such that undrained shear strengths from the latter approach were greater than from the former. The effective strength parameters were determined by plotting the principal stress difference at failure [$t_f = (\sigma_{1f} - \sigma_{3f})/2$] versus the mean of the major and minor principal effective stresses at failure [$s'_f = (\sigma'_{1f} + \sigma'_{3f})/2$], as shown in Figures 9a and 9c for the two failure criteria, respectively. The linear fits to these data produced intercepts of $a' = 0$ and slopes of $\alpha' = 34.5$ and 33.3 degrees, respectively. These parameters were converted to conventional Mohr Coulomb cohesion intercepts (c') and effective friction angles (ϕ') using the following relationships (Lambe and Whitman 1969),

$$c' = \frac{a'}{\cos(\phi')} \tag{1}$$

$$\phi' = \operatorname{asin}\left(\tan\left(\alpha'\right)\right) \tag{2}$$

The resulting strength parameters are $c' = 0$ with $\phi' = 43.4$ and 41.1 degrees, respectively. The critical state friction angle (ϕ'_{cs}) for PM4Silt was subsequently set to 41 degrees, given that the mobilized friction angles were approaching critical state at the larger strains. The undrained shear strengths were equated

with the shear stress on the eventual failure plane at failure (τ_{ff}) and plotted versus the consolidation stress on the eventual failure plane ($\sigma'_{fc} = \sigma'_{3c}$ for ICU tests) as shown in Figures 9b and 9d. The linear fits to these data produced the intercepts (d_R) and slopes (ψ_R) shown on these figures and listed in Table 3; these strength parameters correspond to a consolidation stress ratio $K_c = \sigma'_{1c}/\sigma'_{3c} = 1.0$ since these are ICU tests. The drained strength relationship, defined using $d_S = c'$ and $\psi_S = \phi'$ on a graph of τ_{ff} versus σ'_{fc}, is used to define the undrained shear strength for $K_c = K_f$, where K_f is the maximum possible consolidation stress ratio (i.e., also corresponding to drained failure conditions). Undrained strengths for other values of K_c are linearly interpolated between the strengths estimated for $K_c = 1$ and $K_c = K_f$.

The undrained shear strength at critical state ($s_{u,cs}$) assigned to each zone of PM4Silt was computed using the above procedure and the parameters listed in Table 2 with the initial static consolidation stresses that exist prior to the start of dynamic loading. For each zone, the σ'_{fc} is computed based on the assumption that principle stresses are in the same direction at the time of consolidation and failure (i.e., as is done for rapid drawdown analysis per Duncan and Wright 2005). Additional discussion and examples of this process, including alternative forms and the potential limitations of this procedure for estimating strengths under the more complex loading paths imposed by seismic loading, are provided in Montgomery et al. (2014). The ratio of $s_{u,cs}$ to any consolidation stress becomes excessively large at shallow depths, so $s_{u,cs}$ was limited to be no greater than σ'_{vc} at shallow depths (i.e., $s_{u,cs}/\sigma'_{vc} \leq 1$); this limit avoids depending on large negative pore water pressures during shearing of elements at shallow depths. The $s_{u,cs}$ values produced throughout the embankment by the above procedure are later presented as $s_{u,cs}/\sigma'_{vc}$ contours as an alternative way to view the strengths produced by this adaptation of the Duncan and Wright (2005) procedure. The bounding surface parameter $n^{b,wet}$ was set to 1.0 which eliminates any potential strain-softening during undrained shearing.

A relationship for the small-strain (maximum) shear modulus (G_{max}) was obtained from the results of four resonant column tests by Wahler Associates (1979). The G_{max} values are plotted versus mean

effective consolidation stress (p'_c) in Figure 10, and two alternative fits obtained using the equation for elastic shear modulus used in PM4Silt,

$$G = G_o P_A \left(\frac{p'_c}{P_A} \right)^{n_G} \tag{3}$$

One fit was obtained by fixing the stress exponent $n_G = 0.5$, as generally expected for cohesionless soils, after $G_o = 2{,}640$ was obtained. A second, improved fit was obtained with n_G left as a fitting parameter, which led to $n_G = 0.6$ and $G_o = 2{,}280$. The latter set of parameters were adopted for the PM4Silt calibrations, although the two fits are not significantly different over the range of stresses most important to the dam (i.e., σ'_{vc} of about 1 to 8 atm). Sensitivity analyses presented later include cases with G_o increased or decreased by 30%.

Modulus reduction and equivalent damping ratios for the PM4Silt model were obtained from single element simulations of undrained DSS loading at different strain amplitudes under a range of consolidation stresses. The stress-strain loops obtained for Calibrations 1 and 2, along with the modulus reduction and equivalent damping values from the 3rd loading cycle at each strain amplitude, are shown in Figure 11 for simulations with a consolidation stress of 600 kPa (≈ 6 atm). The stress-strain loops for both calibrations for shear strains up to 1% are approximately the same, despite the differences in their undrained shear strengths. Also shown on this figure are the modulus reduction and equivalent damping ratio relationships recommended by Menq (2003) for a well graded gravel with a coefficient of uniformity (C_u) of 100 and by Vucetic and Dobry (1991) for a fine-grained soil with a PI of 15. The modulus reduction results for PM4Silt are intermediate to these two empirical correlations, which seems appropriate given the embankment materials are well-graded clayey sands and clayey gravels with a PI of about 13. The equivalent damping ratios for PM4Silt are greater than either empirical correlation, which is a common limitation for this model. These simulation results, obtained using the default value for h_o (0.5), were considered sufficiently reasonable that no adjustments to h_o were performed.

The preceding two steps in the calibration process prioritize modeling of the estimated small-strain shear modulus and the modulus reduction and equivalent damping ratio responses over the modeling of the monotonic stress-strain responses from the ICU triaxial tests. The monotonic stress-strain responses from the triaxial tests (Figure 8) have secant shear moduli that are far smaller than from the resonant column test data (Figure 10) and imply shear modulus reduction curves that are shifted well to the left (strong nonlinearity at smaller shear strains) of the empirical relationships shown in Figure 11. Numerous past studies have demonstrated that small-strain properties cannot be reliably measured with conventional triaxial devices due to mechanical compliance, friction, and other limitations, and that laboratory tests on field samples can further underestimate (or sometimes overestimate) the in-situ shear stiffness depending on the degree of sample disturbance, testing procedures, strain levels, and soil type. For example, Lunne et al. (2006) summarize the effects of disturbance and testing procedures on the stress-strain response of soft clays and Boulanger and Wijewickreme (2019) showed how calibration of a constitutive model (PM4Silt) based on in-situ shear wave velocity and empirical shear modulus reduction relationships produced simulated monotonic stress-strain responses that were notably stiffer than those measured in monotonic undrained direct simple shear tests of field samples of a low-plasticity silt. For Austrian Dam, the presence of gravel-sized particles would be expected to exacerbate disturbance associated with field sampling, specimen handling, and laboratory testing, even though relatively large 146-mm diameter samples were used. Volumetric strains during triaxial sample consolidation ranged from 1.8-4.1% (average of 2.5%) which is indicative of relatively poor sample quality, and thus the strain-hardening responses shown in Figure 8 could have been accentuated by sample disturbance effects (e.g., as observed by Lunne et al. 2006 for clays). Simulations of monotonic undrained compression loading using PM4Silt (in plane strain) with the preceding calibration process are compared to the ICU test results for consolidation stresses of 1.02 atm and 3.74 atm in Figures 12a and 12b, respectively. The simulations show the shear strength being almost fully mobilized at shear strains of about 0.5%, after which the stress-strain response is essentially ductile (i.e., the strain-hardening response at larger strains is not simulated). Alternative calibrations that improved simulations of the strain-hardening responses at larger

strains in the ICU triaxial tests produced unrealistic modulus reduction, damping, and cyclic loading responses, and thus the present calibration was considered more appropriate given the limitations inherent to the constitutive model and the uncertainties in soil properties.

Cyclic strengths of the embankment materials were evaluated based on a set of nine anisotropically consolidated undrained (ACU) cyclic triaxial tests by Wahler Associates (1979). These few tests covered three different consolidation stresses, two different anisotropic consolidation stress ratios, samples from the upstream and downstream shells, and different imposed cyclic stress ratios, such that the data were sparse across the testing parameter space. Wahler Associates (1979) developed interpolations across these different parameters using forms consistent with empirical expectations, from which the CSR causing a double-amplitude axial strain of 5% in 30 loading cycles was about 0.25 to 0.28 at consolidation stresses of 3 to 6 atm. These cyclic strengths correspond to about 0.52 to 0.59 times the expected undrained shear strengths based on the first failure criterion. This ratio of cyclic to monotonic strengths is smaller than empirical expectations for a range of clay-like soils (Idriss and Boulanger 2008), although any comparison is complicated by the uncertain relative effects of loading rate (or strain rate) on the cyclic and monotonic strengths of these types of fill materials (cyclic strengths usually determined for the much greater strain rates expected during an earthquake, compared to the standardized strain rates used to determine monotonic strengths). The smaller ratio of cyclic to monotonic strengths could also reflect the differences in soil gradation or the adverse effects of sampling disturbance. In particular, it seems reasonable to anticipate that the unavoidable disturbance associated with sampling this type of material would have a more detrimental effect on its cyclic strengths than its monotonic strengths, which would result in a lower ratio of cyclic to monotonic strength. Given the above concerns and sparseness of the data set, the results of these cyclic test results were considered as likely providing a lower bound on the in-situ cyclic strengths, and thus slightly greater cyclic strength ratios were targeted in the constitutive model calibration described below.

Cyclic strengths for the PM4Silt model were obtained from single element simulations of undrained DSS loading at uniform cyclic stress ratios under a range of consolidation stresses. The cyclic stress-strain

and stress-path responses are illustrated by the results in Figure 13 for Calibration 1 with σ'_{vc} = 6 atm and an initial static shear stress ratios ($\alpha = \tau_{hc}/\sigma'_{vc}$) of 0.0 (Figure 13a) and 0.1 (Figure 13b). These results illustrate the typical cyclic mobility response wherein peak shear strains increased by 1-2% per cycle after the limiting pore pressure conditions had been reached; this rate of shear strain accumulation was obtained by reducing the fabric parameter z_{max}, reducing the fabric growth parameter C_z, and increasing the modulus degradation factor C_{GD} relative to their default values (Table 2). In addition, the results with an initial static shear stress illustrate how the cyclic strength is reduced in the presence of a static shear stress bias and how strains accumulate in the "downslope" direction for these loading conditions. Results of additional simulations with σ'_{vc} = 6 atm and α = 0 are plotted in Figure 14 showing the *CSR* required to cause peak shear strains of 3, 7.5, or 15% at different numbers of uniform loading cycles. The resulting cyclic strength curves are approximately parallel and show that the cyclic strengths for peak shear strains of 3% or 15% are within +/- 5 to 10% of the strengths for a peak shear strain of 7.5%. Note that the *CSR* required to cause a peak shear strain of 3% in thirty cycles is about 0.30, which is intentionally slightly greater than the value estimated from the cyclic testing for the reasons discussed previously. The effect of consolidation stress on cyclic strengths is illustrate by the results for σ'_{vc} = 1, 2, 6, and 12 atm in Figure 15. The *CSR* required to cause a peak shear strain of 7.5% increases with decreasing σ'_{vc} (Figure 15a), but the cyclic strength ratio (τ_{cyc}/s_u) is only slightly affected by the change in σ'_{vc} (Figure 15b). Similar results were obtained for Calibration 2, as illustrated in Figure 16. Both sets of results illustrate that the PM4Silt model provides a reasonable normalization of cyclic and monotonic undrained shear strengths across the range of σ'_{vc} of interest for this embankment.

The two calibrations for PM4Silt (Table 2) primarily differ in their specified undrained shear strengths, with Calibration 1 having lower strengths than Calibration 2. The ICU test data showed strain-hardening responses that could not be reproduced using PM4Silt (e.g., Figure 12) without sacrificing other key features of behavior. For this reason, the intent is that Calibration 1 may be viewed as appropriate for loading conditions that produce peak shear strains of only a few percent, whereas

Calibration 2 is more appropriate for loading conditions that cause peak shear strains in the range 10-20%. Repeating the NDAs with both calibrations provides an assessment of the sensitivity of the computed deformations to this aspect of how undrained shear strengths are selected.

INITIAL STATIC STRESS AND SEEPAGE CONDITIONS

The analyses for initial static stress and seepage conditions, as well as for dynamic loading, were performed using the two meshes in Figure 6 with the finite difference software FLAC 8.0 (Itasca 2016); the initial static stress and seepage conditions in the embankment were essentially identical with or without the inclusion of the bedrock layer, and thus results are only presented for the mesh in Figure 6a. The initial static stress and seepage conditions were established through the following sequence of analysis steps. The initial seepage conditions were established first using an uncoupled analysis. The initial static stresses were then computed using another uncoupled analysis (with water pressures fixed at the values obtained in the preceding analysis) in which: (1) vertical total stresses were initiated based on the vertical column of overlying soils, (2) horizontal effective stresses were initiated based on a K_o of 0.50, (3) all zones were assigned a Mohr Coulomb material model with drained strengths and confinement-dependent secant shear moduli, and (4) equilibrium was then solved for. If necessary, initial horizontal stresses in individual zones were adjusted to keep K_o values between 0.4 and 2.5, and equilibrium solved for again. The material model was then switched to PM4Silt and equilibrium solved for again. Lastly, the analysis was switched to a coupled mode and equilibrium solved for one last time. The last two solutions for equilibrium serve as a check that everything has been specified correctly; i.e., equilibrium stresses were relatively unaffected by these steps and convergence was almost immediate. The initial static stress conditions produced by this procedure were then evaluated for reasonableness, as discussed below.

The results of the steady seepage analysis are illustrated by the pore pressure contours and phreatic surface shown in Figure 17. Hydraulic conductivities for the three regions of the model were iteratively adjusted to produce a phreatic line that matched with the levels measured in piezometer P-6 (at dam centerline) and piezometers P-1 and P-2 (nearest the downstream toe). The first analysis case assumed:

(1) the vertical hydraulic conductivity in the impervious zone was 10^{-5} cm/s, (2) the vertical hydraulic conductivities in the pervious and gravel strip drain zones were 10 and 100 times the vertical conductivities of the impervious zone, respectively, and (3) the horizontal hydraulic conductivities were 2 times the vertical conductivities for all zones. The final calibrated analysis case assumed: (1) the vertical hydraulic conductivities in the impervious and pervious zones were both 10^{-5} cm/s and 2 times greater in the strip drain zone, and (2) the horizontal hydraulic conductivities were 1, 10, and 12 times the vertical conductivities in the pervious, impervious, and strip drain zones, respectively. The increased horizontal hydraulic conductivity in the upstream impervious zone was required for obtaining agreement with the phreatic surface measured at P-6. The simulated phreatic surface at piezometer P-4 (midway between the others) is above its measured level, which was unavoidable given that the level measured at P-4 was lower than that measured further downstream in P-1 and P-2. Overall, the seepage analysis results are considered sufficiently consistent with the piezometer data for establishing the initial static stresses within the embankment, while recognizing that the calibrated hydraulic conductivities are undoubtedly compensating for other limitations of the numerical model, including not accounting for seepage in the bedrock or potential layering within the compacted embankment.

The initial static stress conditions are illustrated in Figure 18 with contours of σ'_v (Figure 18a), K_o (Figure 18b), and α (Figure 18c). Total unit weights for unsaturated and unsaturated zones were 19.1 and 21.8 kN/m^3, respectively. The σ'_v vary smoothly with distance from the surface of the dam, and reach maximum values of about 8 atm along the bedrock immediately below the crest. The K_o values range from 0.4 to 0.6 throughout the central portion of the dam, and increase to values greater than unity at shallow depths along the upstream and downstream faces. This pattern of K_o values is considered reasonable because compaction-induced stresses would be expected to produce greater K_o values at shallower depths (perhaps the upper 6 m), whereas K_o values at the greater depths in the central portion of the embankment would be expected to be closer to normally-consolidated values. The α values are less than 0.2 through the central portion of the dam and less than 0.3 everywhere except at shallow depths

along the upstream and downstream faces. These results are considered a reasonable estimate of stress conditions within the embankment prior to the earthquake.

The $s_{u,cs}$ values assigned to PM4Silt based on the initial static stress conditions are shown as contours of equivalent $s_{u,cs}/\sigma'_{vc}$ in Figure 19. The $s_{u,cs}/\sigma'_{vc}$ ratios range from 0.35 to 0.5 throughout the central portion of the dam, and increase to values as large as 1.0 at shallow depths. Sensitivity analyses showed that the $s_{u,cs}$ values are relatively insensitive to variations in K_o produced by alternative approaches to establishing initial static stress conditions; in effect, the procedure for computing $s_{u,cs}$ was found to be most strongly controlled by the major principal effective stress and only slightly influenced by the minor principal effective stress for this embankment.

The soil above the phreatic surface is modeled as unsaturated with zero pore pressure, which corresponds to assuming drained strengths during static and dynamic loading. In reality, the soils may remain almost saturated to some height above the phreatic surface and be partially saturated everywhere else above the phreatic surface. Negative pore pressures above the phreatic surface would be expected to strengthen the soil, whereas saturation above the phreatic surface may weaken the soil because it can more easily generate positive pore pressures during earthquake loading. The above two effects may be partly compensating in how they affect the overall dam response. The assumption of drained conditions above the phreatic surface is nonetheless common in practice, and thus its use herein is consistent with the intent of the present study. Sensitivity analyses presented later include cases with the zone of saturation extending 3 to 6 m above the phreatic surface due to capillary rise.

DYNAMIC SIMULATION RESULTS

Dynamic analyses were performed using the two PM4Silt calibrations and all four input motions. Results are presented first for the mesh with a rigid foundation (Figure 6a), while results for the mesh with a 60-m-thick bedrock layer (Figure 6b) are presented later as part of the sensitivity analyses. All analyses were performed in large deformation mode and were coupled with the pore fluid, although with no pore fluid flow during dynamic loading. The horizontal input motions (Figure 4) were applied in combination with the vertical component of motion recorded at the same strong motion station (the effect

of omitting the vertical component of motion is discussed later). The horizontal and vertical motions were applied directly to the base of the model with a rigid foundation (Figure 6a). Rayleigh damping of 0.5% at a frequency of 1.0 Hz was used during dynamic loading. Detailed results are presented for Calibration 1 with the Corralitos Channel 1 input motion (i.e., the station with the most similar epicentral distance and the component that closely aligns with the transverse loading direction for Austrian Dam), after which the results of other analysis cases are summarized.

Results for Calibration 1 with the Corralitos Channel 1 Input Motion

Time series of acceleration at the bedrock and dam crest, horizontal and vertical displacement at the dam crest (relative to the bedrock), and excess pore pressure head at three locations in the embankment for Calibration 1 and the Corralitos Channel 1 input motion are shown in Figure 20. The horizontal accelerations at the dam crest are significantly amplified relative to the input motion, reaching peak values of 0.7g several times, and decay more slowly with time than the input motion. The dam crest settles more than 900 mm in the first 10 s, and then slowly increases to 1,060 mm at the end of strong shaking. The dam crest also develops a horizontal upstream displacement of about 94 mm at the end of strong shaking. Excess pore pressure heads at the end of strong shaking were 18.1 m at the location of P-1, 5.0 m at the location of P-6, and 17.8 m at a point B-6 located halfway between P-6 and the underlying bedrock. The analysis was continued for sufficient time after the end of strong shaking to allow for full dissipation of excess pore water pressures, during which the crest settlements increased by less than 1%, which is consistent with the survey data showing that crest settlements did not increase measurably with time after the earthquake.

Contours of horizontal and vertical displacement, shear strain, and excess pore pressure at the end of strong shaking are shown in Figures 21a, 21b, 21c, and 21d, respectively. The displacement patterns indicate a relatively symmetric slumping of the embankment with rotational components of deformation on both the upstream and downstream faces. The crest settlement is 1,060 mm and the mid-faces of the upstream and downstream faces move laterally by about 800 mm. Shear strains are less than 5% throughout most of the embankment, but increase to maximum values of 10-25% near the embankment-

bedrock interface beneath the upstream and downstream shells. The larger shear strains in the saturated portion of the downstream shell are qualitatively consistent with the observed deformation of the tubing for piezometer P-1 at about 7.6 to 9.1 m above the bedrock, given that the model did not account for any increased strength in the gravel strip drain zone which would have likely caused the zone of greatest shear strains to be above the drain zone. The shear strain and vertical displacement contours show relatively small deformations in the lower central portion of the embankment and an increased gradient of deformations near mid-height beneath the dam crest, which are again qualitatively consistent with observed deformation of the tubing for piezometer P-6 near mid-height below the dam crest. The shear strains in most of the saturated zone are more consistent with the shear strains associated with the failure criterion used for developing Calibration 1 than Calibration 2, whereas the maximum shear strains near the bedrock contact are getting closer to being consistent with the criterion used for developing Calibration 2. The excess pore pressures in much of the saturated zone are 150-200 kPa, with maximum values of about 300 kPa in a more limited zone near the bedrock contact just downstream of the centerline. These excess pore pressures correspond to excess heads (i.e., rises in piezometer levels) of 15-30 m. The excess pore pressure heads decrease rapidly near the phreatic surface, indicating that the excess heads computed at points in these areas will be sensitive to where the phreatic surface develops during the seepage analyses.

Results for Both Calibrations and All Input Motions

Settlement of the dam crest from the NDAs with each calibration and input motion are summarized in Table 4, along with the maximum measured settlement. The computed crest settlements with either of the Corralitos input motions (Channel 1 or 3) were similar for either calibration of PM4Silt; i.e., 1,048-1,060 mm with Calibration 1 and 822-874 mm with Calibration 2. The computed crest settlements with either of the Lenihan input motions (Channel 1 or 3) were also similar for either calibration (840-853 mm for Calibration 1 and 610-638 mm for Calibration 2), and were about 20-25% smaller than those obtained with the Corralitos motions. For either set of input motions, the crest settlements for Calibration 2 were about 20-25% smaller than obtained with Calibration 1. The patterns of deformation were generally

similar for all motions and both calibrations, as illustrated by comparing the contours of horizontal displacement obtained with Calibration 2 and the Corralitos Channel 1 input motion (Figure 22) with those shown previously in Figure 21b (Calibration 1 and same input motion). The maximum measured crest settlement of 859 mm is about equal to the average of all the computed values, at the lower end of values computed with Calibration 1, and at the upper end of values computed with Calibration 2.

Horizontal displacement of the dam crest (near the centerline) at the end of strong shaking ranged from 202 mm upstream to 36 mm downstream for these eight analysis cases summarized in Table 4. The horizontal displacements are small relative to the vertical crest settlements, which is consistent with the general symmetry of deformations in the upstream and downstream shells. The dam crest also experienced horizontal extensional strains, such that horizontal displacements at the crest edges generally differed from those at the centerline by 20-50 mm. The measured horizontal crest displacements were more varied (130 mm upstream to 330 mm downstream) and uncertain given concerns over the reference benchmark (Harder et al. 1998). The computed horizontal displacements are reasonable in magnitude but appear biased toward the upstream direction compared to the measurements; possible causes for this bias in deformation direction include the characteristics of the input motions or the assumption of identical properties for the upstream and downstream zones.

The excess pore pressure heads computed at points P-1, P-2, P-4, P-6 and B-6 at the end of strong shaking with each calibration and input motion are summarized in Table 5, along with the measured values. The excess heads computed at P-1 with Calibration 1 (15.1-19.6 m) are consistent with the measured excess head (16.8 m), whereas the values computed with Calibration 2 (10.0-13.3 m) under-estimate the measured excess head. The excess heads computed at P-2 with either Calibration (6.6-11.3 m) are all greater than measured (2.7 m), and the excess heads computed at P-4 with either Calibration (6.3-12.2 m) are also similarly greater than measured (4.0 m). The excess heads computed at P-6 with either Calibration (2.5-6.9 m) are well below the measured value (15.2 m), but the excess head at the lower B-6 (11.2-19.5 m) are similar to those measured just above it at P-6. Overall, the computed excess heads in the saturated zone are reasonably consistent with the general magnitude of the measured values,

allowing for uncertainties in the field measurements and the variation of computed values with the input motion, model calibration, and exact position of the sensing interval relative to the phreatic surface.

The displacement patterns obtained in all analysis cases are also qualitatively consistent with the cracking and bulging patterns observed in the field. The contours of computed horizontal displacement (e.g., Figures 21a and 22a) have large horizontal extensional gradients on the upstream and downstream faces just below the dam crest, which correspond closely with the areas where longitudinal cracking was observed on both faces (Figure 1). The contours of horizontal displacement also have large horizontal compressive gradients along the lower portions of both faces, which correspond closely with the area where bulging was observed on the downstream face (Figures 1 and 5b); note that similar bulging along the lower portion of the upstream face would have been below the reservoir level and may have gone unobserved.

The eight analysis cases in Tables 4 and 5 were repeated with the vertical component of the input motion omitted to evaluate the effect of that common simplification in practice. The dam crest settlements for Calibrations 1 and 2 were reduced by 9-14% (average 12%) for the Corralitos input motions and 4-8% (average 5%) for the Lenihan input motions. The simulated excess pore pressure heads at the piezometer locations instead increased by about 0.7 m on average, with the excess heads at individual piezometers increasing or decreasing by as much a 3 m depending on the calibration and motion. These differences in deformations and pore pressures are small enough that the general agreement between measured and computed responses is not significantly affected by including or omitting the vertical component of the bedrock input motion.

Sensitivity of Results to Other Model Variations

The effect of several other model variations on computed dam crest settlements are summarized in Table 6. The baseline analysis case for this table was the rigid foundation model with Calibration No. 1 and the Corralitos Channel 1 recording as the horizontal input motion.

- Recalibrating PM4Silt with G_o increased by 30% caused the crest settlement to decrease by 9%, whereas recalibrating with G_o decreased by 30% caused crest settlement to increase by 18%.

These two recalibrations included reducing h_{po} to 30 (from the baseline 40) and increasing h_{po} to 55, respectively, to maintain the same cyclic strengths as the baseline case. Thus, the effect of changing G_o is primarily attributed to its effect on the dam's dynamic response.

- Reversing the polarity of the horizontal motion caused crest settlement to decrease by 3%. The small effect of polarity is reasonable given the general symmetry of the dam and input motion.
- Extending the saturated zone 3 m above the phreatic surface caused crest settlement to decrease by 4%, and extending it 6 m above the phreatic surface cause it to decrease by 7%. This relatively small net effect is attributed to the compensating effects that saturation and negative initial pore pressures above the phreatic surface have on the monotonic and cyclic strengths at different overburden stresses.
- Increasing the total unit weights to 20.9 kN/m3 above the phreatic surface (a 9% increase to account for possibly higher water contents) and 22.1 kN/m^3 below the phreatic surface (a 1.4% increase) caused crest settlement to decrease by 2%. The small effect on crest displacements is reasonable given the various compensating effects that total unit weight has on consolidation stresses, strengths, fundamental periods, and driving stresses.
- Including a 60-m-thick layer of bedrock with a compliant base and free-field side boundary conditions (Figure 6b) caused crest settlement to decrease by 29%, 18%, and 9% when the bedrock was assigned a shear wave velocity of 1,000 m/s, 2,000 m/s, and 4,000 m/s, respectively. The effect of the bedrock layer decreases with increasing rock stiffness, since the stiffer rock is closer to approximating the rigid foundation condition assumed for the baseline case.

The crest settlements ranged from 750 mm to 1,250 mm for all of the above sensitivity analysis cases, and ranged from 750 mm to 867 mm for the cases with a bedrock layer having a shear wave velocity of 1,000 m/s or 2,000 m/s. The latter analysis results are particularly relevant, given that shear wave velocities in the Franciscan formation bedrock at Austrian Dam could very reasonably fall within this range. These latter analysis results are still consistent with the observed maximum crest settlement of 859 mm, whereas

similar analyses using the stronger Calibration No. 2 and the less damaging Lenihan input motions (Table 4) would have underestimated the observed crest settlements.

DISCUSSION

Sources of potential bias or dispersion in NDA results for embankment dams, including those presented herein for Austrian Dam, include uncertainties associated with the initial conditions (e.g., stresses, pore pressures, saturation levels), material properties (e.g., spatial variability, sample disturbance, shearing mode), constitutive models (e.g., calibration, limitations), numerical modeling procedures, and input motions. For this reason, case history studies provide an invaluable check that the aggregation of all the steps involved in any NDA modeling procedure produce an outcome that is reasonably consistent with the observed field performance. The comparisons of predicted and measured responses over several case histories provide a sense of potential bias or dispersion for future applications of the same NDA modeling procedures, recognizing that good agreement for any one case history could be due to a number of compensating errors and poor agreement for any one case history could be due to accumulation of several smaller errors.

The characterization and constitutive modeling of the compacted clayey sand and clayey gravel fill materials were of particular concern for the present case history study. These types of compacted fills are difficult to sample and the available laboratory tests showed strain-hardening behaviors that are difficult to model with existing constitutive models. The PM4Silt model produced simulated responses that were reasonably consistent with the available characterization data, but the effect of strain-hardening on the undrained strength at large shear strains could only be enveloped by developing two alternative strength/model calibrations. Furthermore, the estimated in-situ undrained shear strengths include uncertainties associated with: (1) the effects of sampling disturbance, (2) the unknown effects of loading rate on the shear strength of these types of intermediate soils during an earthquake, (3) the use of the procedures from Duncan and Wright (2005) for estimating undrained shear strengths based on anisotropic consolidation stresses, and (4) other factors such as fill age, inherent anisotropy, loading path, prior stress history, partial saturation, and cementation. The procedures used herein to characterize the strengths of

the compacted fills are considered representative of common engineering practices, and the two different strength representations and corresponding constitutive model calibrations provide insight on how uncertainty in shear strengths can affect predicted responses.

CONCLUSIONS

Two-dimensional NDAs of Austrian Dam in the 1989 M_w=6.9 Loma Prieta Earthquake were performed using the finite difference program FLAC 8.0 (Itasca 2016) with the user-defined constitutive model PM4Silt (Boulanger and Ziotopoulou 2018) and engineering procedures common in practice. This relatively homogenous, 55-m high embankment dam was comprised primarily of compacted low-plasticity clayey sands and clayey gravels. The dam developed extensive cracking, crest settlements up to 859 mm, and excess pore pressure heads up to 16.8 m due to the strong shaking with estimated peak horizontal bedrock accelerations of 0.4-0.6g. The engineering properties of the compacted embankment materials were reevaluated based on the isotropically consolidated undrained triaxial compression and resonant column test data by Wahler Associates (1979, 1981). Two alternative interpretations of the compacted fill's undrained shear strength data were developed and used to produce two alternative calibrations for the PM4Silt model.

The embankment responses computed for the two alternative PM4Silt calibrations (and hence undrained strength representations) and four different input motions were in reasonable agreement with, and generally bounded, the observed crest settlements, embankment deformation patterns, and excess pore pressures. For example, the eight different analysis cases listed in Table 4 produced crest settlements that ranged from 610-1,060 mm (-29% to +23% from the measured 859 mm) and averaged 843 mm (within 2% of the measured value). Similarly, the nine sensitivity analysis cases using Calibration No. 1 with the Corralitos Channel 1 input motion (Table 6) produced crest settlements that ranged from 750-1,250 mm (-13% to +46% from the measured 859 mm). The results of this case history study provide support for the use of these analysis methods and engineering procedures in seismic evaluations of compacted earthfill embankments.

DATA AVAILABILITY STATEMENT

Some or all data, models, or code generated or used during the study are available in a repository or online in accordance with funder data retention policies. The manual, dynamic link library, and example calibration files for PM4Silt are available at https://pm4silt.engr.ucdavis.edu/.

ACKNOWLEDGMENTS

The work described herein progressed under projects for the California Division of Safety of Dams under Contract 4600009523, the Department of Water Resources under Contract 4600009751, and the National Science Foundation under grant CMMI-1635398. Any opinions, findings, conclusions, or recommendations expressed herein are those of the author and do not necessarily represent the views of these organizations. The anonymous reviewers provided valuable suggestions for additional analyses and broader discussions that significantly improved the paper. The author appreciates the above support and suggestions.

APPENDIX A. UNDRAINED SHEAR STRENGTH ASSIGNMENT

The assignment of the undrained shear strength at critical state ($s_{u,cs}$) to an element (or zone) of PM4Silt in the numerical model is based on the initial static consolidation stress conditions that exist just prior to dynamic loading. The $s_{u,cs}$ for each zone is computed using the procedures described in Duncan and Wright (2005) for limit equilibrium slope stability analyses and extended to finite element or finite difference models by Montgomery et al. (2014). The sequence of calculations for each individual element/zone in the numerical model is described below.

The initial vertical and horizontal effective stresses (σ'_v, σ'_h) and the horizontal shear stress (τ_{vh}) in the plane section of the 2D model are used to compute the major and minor principal effective stresses at consolidation (σ'_{1c}, σ'_{3c}) as,

$$\sigma'_{1c} = \frac{\sigma'_v + \sigma'_h}{2} + \left[\left(\frac{\sigma'_v - \sigma'_h}{2} \right)^2 + \left(\tau_{vh} \right)^2 \right]^{1/2} \quad \text{(A1)}$$

$$\sigma'_{3c} = \frac{\sigma'_v + \sigma'_h}{2} - \left[\left(\frac{\sigma'_v - \sigma'_h}{2} \right)^2 + \left(\tau_{vh} \right)^2 \right]^{1/2} \quad \text{(A2)}$$

The consolidation stress ratio (K_c) is,

$$K_c = \frac{\sigma'_{1c}}{\sigma'_{3c}} \quad \text{(A3)}$$

The consolidation stress on the eventual failure plane (σ'_{fc}) is computed assuming the orientation of the failure plane is the same at consolidation and failure (Lowe and Karafiath 1960),

$$\sigma'_{fc} = \frac{\sigma'_{1c} + \sigma'_{3c}}{2} - \frac{\sigma'_{1c} - \sigma'_{3c}}{2} \sin(\phi') \quad \text{(A4)}$$

The shear stress on the eventual failure plane at failure (τ_{ff}) for consolidation at K_c =1 is computed using the undrained shear strength parameters developed from the ICU test data as,

$$\tau_{ff,K_c=1} = d_R + \sigma'_{fc} \tan\left(\psi_R\right) \quad \text{(A5)}$$

The shear stress on the eventual failure plane at failure for consolidation at $K_c = K_f$ is computed using the effective stress shear strength parameters and noting that $\sigma'_{ff} = \sigma'_{fc}$ for this case,

$$\tau_{ff,K_c=K_f} = c' + \sigma'_{fc} \tan(\phi') \quad \text{(A6)}$$

The value of K_f depends on the consolidation stresses and is computed as,

$$K_f = \frac{\sigma'_{1f}}{\sigma'_{3f}} = \frac{\frac{\tau_{ff} - c'}{\tan(\phi')} + \tau_{ff} \tan(\phi') + \frac{\tau_{ff}}{\cos(\phi')}}{\frac{\tau_{ff} - c'}{\tan(\phi')} + \tau_{ff} \tan(\phi') - \frac{\tau_{ff}}{\cos(\phi')}} \quad \text{(A7)}$$

The shear stress on the eventual failure plane at undrained failure for consolidation at any other value of K_c is linearly interpolated from the undrained strengths for K_c = 1 and $K_c = K_f$ as,

$$\tau_{ff,K_c} = \tau_{ff,K_c=1} + \frac{\left(\tau_{ff,K_f} - \tau_{ff,K_c=1} \right)}{\left(K_f - 1 \right)} (K_c - 1) \quad \text{(A8)}$$

The $s_{u,cs}$ for PM4Silt may then be assigned in one of two ways. One option is to set $s_{u,cs} = \tau_{ff,K_c}$ while recognizing that this introduces a degree of conservatism because $s_{u,cs}$ corresponds to the maximum shear

stress at critical state rather than the shear stress on the eventual failure plane. The second option is to set $s_{u,cs} = \tau_{ff,K_c} / \cos(\phi'_{cv})$ which converts τ_{ff,K_c} to a maximum shear stress for consistency with $s_{u,cs}$. The first option was used for the present analyses to maintain consistency with common practices for evaluating slope stability (e.g., Duncan and Wright 2005), while recognizing that others may prefer the second option.

For the analyses of Austrian Dam, the second option for specifying $s_{u,cs}$ would give a 33% increase in strength compared to the first option because of the relatively large critical state friction angle. A 33% increase in strength is greater than the differences in strengths obtained using Calibration No. 2 versus Calibration No. 1; the strengths obtained with Calibration No. 2 are generally 10-30% greater than with Calibration No. 1, with the difference varying throughout the embankment as the consolidation stress and consolidation stress ratio vary. The best agreement between computed and observed dam responses for cases that included a compliant bedrock layer was generally obtained using Calibration No. 1 with the first option for specifying $s_{u,cs}$, and thus use of the second option would be expected to result in an under-estimation of dam deformations given the other assumptions and modeling choices made for these analyses.

REFERENCES

Babbitt, D. H. (1991). Memorandum of field review, Austrian Dam, No. 622-113, Performance during and after October 17, 1989 earthquake. Revised September 5. California Division of Safety of Dams.

Boulanger, R. W., Price, A. B., and Ziotopoulou, K. (2018). "Constitutive modeling of the cyclic loading response of low plasticity fine-grained soils." GSIC 2018, Proc. GeoShanghai 2018 International Conference: Fundamentals of Soil Behaviours, A. Zhou et al. (Eds.), Springer Nature Singapore Pte Ltd., pp. 1–13, https://doi.org/10.1007/978-981-13-0125-4_1.

Boulanger, R. W., and Wijewickreme, D. (2019). "Calibration of a constitutive model for the cyclic loading responses of Fraser River Delta Silt." Proc., VII International Conference on Earthquake Geotechnical Engineering, Rome, Italy, June 17-20.

Boulanger, R. W., and Ziotopoulou, K. (2018). "PM4Silt (Version 1): A silt plasticity model for earthquake engineering applications." Report No. UCD/CGM-18/01, Center for Geotechnical Modeling, Department of Civil and Environmental Engineering, University of California, Davis, CA.

CESMD (2019). Center for Engineering Strong Motion Data, https://strongmotioncenter.org/, Accessed April 12, 2019.

Duncan, J. M., and Wright, S. G. (2005). Soil Strength and Slope Stability, John Wiley and Sons, Inc.

Elia, G., and Rouainia, M. (2013). "Seismic performance of earth embankment using simple and advanced numerical approaches." Journal of Geotechnical and Geoenvironmental Engineering, ASCE 139(7): 1115-1129.

Gibbs, J.F., Fumal, T.E., and Powers, T.J. (1993). Seismic velocities and geologic logs from borehole measurements at eight strong motion stations that recorded the 1989 Loma Prieta, California, earthquake, OFR 93-376, U.S. Geological Survey, Menlo Park, CA.

Hadidi, R., Moriwaki, Y., Barneich, J., Kirby, R., and Mooers, M. (2014). "Seismic deformation evaluation of Lenihan Dam under 1989 Loma Prieta Earthquake." Tenth US National Conference on Earthquake Engineering, Frontiers of Earthquake Engineering, July 21-25, Anchorage, Alaska.

Harder, L. F., Jr., Bray, J. D., Volpe, R. L., and Rodda, K. V. (1998). "Performance of earth dams during the Loma Prieta earthquake." US Geological Survey Professional Paper 1552-D, T. L. Holzer ed., US Geological Survey, 3-26.

Idriss, I. M., and Boulanger, R. W. (2008). Soil liquefaction during earthquakes. Monograph MNO-12, Earthquake Engineering Research Institute, Oakland, CA, 261 pp.

Itasca (2016). FLAC, Fast Lagrangian Analysis of Continua, User's Guide, Version 8.0. Itasca Consulting Group, Inc., Minneapolis, MN.

Lambe, T. W. and Whitman, R. V. (1969). *Soil Mechanics.* John Wiley and Sons, Inc.

Lowe, J. and Karafiath, L. (1960). "Effect of anisotropic consolidation on the undrained shear strength of compacted clays." *Proc., Research Conference on Shear Strength of Cohesive Soils*, Boulder, Colo., June, 837-858.

Lunne, T., Berre, T., Andersen, K. H., Strandvik, S., & Sjursen, M. 2006. Effects of sample disturbance and consolidation procedures on measured shear strength of soft marine Norwegian clays. Canadian Geotechnical Journal, 43: 726-750.

Luque, R., and Bray, J. D. (2017). "Dynamic analyses of two buildings founded on liquefiable soils during the Canterbury Earthquake Sequence." Journal of Geotechnical and Geoenvironmental Engineering, ASCE, 143(9): 04017067.

Makdisi, F. I., Chang, C. Y., Wang, Z. L., and Mok, C. M. (1991). "Analysis of the recorded response of Lexington Dam during various levels of ground shaking." SMIP91 Seminar Proceedings, Strong Motion Instrumentation Program, California Division of Mines and Geology, paper 10.

Mejia, L. H., Sun, J. I., Salah-Mars, S., Moriwaki, Y., and Beikae, M. (1992). "Nonlinear dynamic response analysis of Lexington Dam." SMIP92 Seminar Proceedings, Strong Motion Instrumentation Program, California Division of Mines and Geology, paper 10.

Menq, F.H. (2003). Dynamic properties of sandy and gravelly soils. PhD Dissertation, University of Texas at Austin.

Montgomery, J., Boulanger, R. W., Armstrong, R. J., and Malvick, E. J. (2014). "Anisotropic undrained shear strength parameters for non-linear deformation analyses of embankment dams." Geo-Congress 2014: Geo-Characterization and Modeling for Sustainability, Geotechnical Special Publication 234, ASCE Geo-Institute, 1294-1306.

Rampello, S., Cascone, E., and Grosso, N. (2009). "Evaluation of the seismic response of a homogenous earth dam." Soil Dynamics and Earthquake Engineering, 29, 782-798, 10.1016/j.soildyn.2008.08.006.

Stark, T. D., Beaty, M. H., Byrne, P. M., Castro, G., Walberg, F. C., Perlea, V. G., Axtell, P. J., Dillon, J. C., Empson, W. B, and Mathews, D. L. (2012). "Seismic deformation analysis for Tuttle Creek Dam." Canadian Geotechnical Journal, 49: 323-343.

Vrymoed, J., and Lam, W. (2006). "Earthquake performance of Austrian Dam, California during the Loma Prieta Earthquake." ASDSO.

Vucetic, M., and Dobry, R. (1991). "Effect of soil plasticity on cyclic response." Journal of Geotechnical Engineering, 117(1), 89–107.

Wahler Associates (1979). "Initial Evaluation of Seismic Stability of Austrian Dam, December, 1979," File No. 622-13, Item No. 8, California Department of Water Resources, Division of Safety of Dams.

Wahler Associates (1981). "Seismic Safety Evaluation of Austrian Dam For San Jose Water Works, August 1981," File No. 622-13, Item No. 10, California Department of Water Resources, Division of Safety of Dams.

Wahler Associates (1990). Austrian Dam-Investigation and remedial construction following the October 17, 1989 Loma Prieta Earthquake: Report prepared for the San Jose Water Company.

Wald, D. J., Helmberger, D. V., and Heaton, T. H. (1991). "Rupture model of the 1989 Loma Prieta Earthquake from the inversion of strong-motion and broadband teleseismic data." Bulletin of Seismological Survey of America, 81(5): 1540-1572.

Ziotopoulou, K., and Boulanger, R. W. (2016). "Plasticity modeling of liquefaction effects under sloping ground and irregular cyclic loading conditions." Soil Dynamics and Earthquake Engineering, 84 (2016), 269-283, 10.1016/j.soildyn.2016.02.013.

Table 1: Classification and compaction data for embankment materials (Wahler Associates 1979, 1981)

Property	Range	Mean
USCS classification	SC, GC	--
Percent coarser than No. 4 sieve (%)	26 – 72	46
Percent finer than No. 200 sieve (%)	16 – 44	32
Specific gravity, G_s	2.60 – 2.78	2.70
Liquid Limit, LL	28 – 32	31
Plasticity Index, PI	11 – 15	13
Water content as compacted in ~1950 (%)	9.5 – 19.5	14.5
Dry unit weight as compacted in ~1950 (kN/m^3)	16.90 – 20.75	19.04
Dry unit weight of samples in ~1989 (kN/m^3)	19.07 – 20.69	19.90

Table 2. Input parameters for PM4Silt calibrations

Input parameter	Default value	Calibration No. 1	Calibration No. 2
$s_{u,cs}$ – s_u at critical state	-- [a]	$f(\sigma'_{fc}, K_c)$ [b]	
G_o – shear modulus coefficient	-- [a]	2280	
h_{po} – contraction rate parameter	-- [a]	40	80
n_G – shear modulus exponent	0.75	0.6	
h_o – plastic modulus ratio	0.5	-- [c]	
e_o – initial void ratio	0.9	0.394	
λ - compressibility in e-ln(p') space	0.06	-- [c]	
ϕ'_{cv} – critical state friction angle	32°	41°	
$n^{b,wet}$ – bounding surface parameter	0.8	1.0	
$n^{b,dry}$ – bounding surface parameter	0.5	-- [c]	
n^d – dilation surface parameter	0.3	-- [c]	
A_{do} – dilatancy parameter	0.8	-- [c]	
$r_{u,max}$ – sets bounding p_{min}	$p_{min} = p_{cs}/8$	-- [c]	
z_{max} – fabric term	$10 \le 40(s_u/\sigma'_{vc}) \le 20$	5	
C_z – fabric growth parameter	100	50	
C_ε - strain accumulation rate factor	$0.5 \le (1.2s_u/\sigma'_{vc}+0.2) \le 1.3$	-- [c]	
C_{GD} –modulus degradation factor	3.0	6.0	
$C_{k\alpha f}$ – plastic modulus factor	4.0	-- [c]	
ν_o – Poisson ratio	0.3	-- [c]	

[a] Required input parameter that does not have a default value.

[b] Computed using the strength parameters in Table 3.

[c] Retained default value.

Table 3. Undrained shear strength parameters from reinterpretation of the ICU triaxial compression test data in Wahler Associates (1981)

Consolidation condition	Strength parameter	Calibration 1	Calibration 2
K_c =1 (ICU)	d_R	0.37 atm	0.54 atm
	ψ_R	22.4°	28.6°
$K_c = K_f$	d_S (= c')	0 atm	0 atm
	ψ_S (= ϕ')	43.4°	41.1°

Table 4. Dam crest settlements – measured and computed using the baseline model

Case	Peak horizontal base accel. (g)	Dam crest settlement (mm) Calibration 1	Calibration 2
Measured [a]	n.a.	859	
Corralitos - Chan 1 [b,c]	0.479	1060	822
Corralitos - Chan 3 [b]	0.630	1048	874
Lenihan - Chan 1 [b,c]	0.410	840	610
Lenihan - Chan 3 [b]	0.442	853	638

[a] Survey data as reported in Harder et al. (1998)

[b] Recording station and horizontal component used for the input motion. The vertical component of the input motion was Channel 2 from the same recording station.

[c] Horizontal recording is oriented due east, which is approximately transverse to Austrian Dam.

Table 5. Increases in piezometer levels due to earthquake loading – measured and computed using the baseline model

Case	Input motion	Piezometer rise due to earthquake loading (m) P-1	P-2	P-4	P-6 (B-6)[a]
Measured [b]	n.a.	16.8	2.7	4.0	15.2
Calibration 1	Corralitos – Chan 1 [c]	18.1	11.3	10.9	5.0 (17.8)
	Corralitos – Chan 3 [c]	19.6	11.0	10.8	5.8 (19.5)
	Lenihan – Chan 1 [c]	16.1	7.3	11.5	6.0 (13.7)
	Lenihan – Chan 3 [c]	15.1	7.2	12.2	6.9 (14.6)
Calibration 2	Corralitos – Chan 1 [c]	13.1	7.2	8.9	2.5 (13.8)
	Corralitos – Chan 3 [c]	13.3	7.6	10.0	2.5 (15.9)
	Lenihan – Chan 1 [c]	10.0	6.6	6.3	4.8 (11.2)
	Lenihan – Chan 3 [c]	11.1	6.7	8.2	4.9 (11.2)

[a] Piezometer 6 is located just below the simulated phreatic surface; Excess pore pressures increase significantly just below this elevation, so computed values for point B-6 midway between P-6 and the bedrock surface are reported in parenthesis.

[b] Recorded October 19, 2018 by Wahler Associates (1990)

[c] Recording station and horizontal component used for the input motion. The vertical component of the input motion was Channel 2 from the same recording station.

Table 6. Sensitivity of computed dam crest settlements to numerical model variations

Variation from the baseline model	Dam crest settlement (mm)	Change from baseline
Baseline case [a]	1060	--
Embankment G_o increased 30% [b]	967	-9%
Embankment G_o decreased 30% [c]	1,250	18%
Reverse polarity of horizontal component	1,027	-3%
Saturation extended 3 m above phreatic surface	1,015	-4%
Saturation extended 6 m above phreatic surface	981	-7%
Increase unit weight to 20.9 kN/m^3 above, and 22.1 kN/m^3 below, the phreatic surface, respectively	1041	-2%
Bedrock included, with $V_{s,rock}$ = 1,000 m/s	750	-29%
Bedrock included, with $V_{s,rock}$ = 2,000 m/s	867	-18%
Bedrock included, with $V_{s,rock}$ = 4,000 m/s	962	-9%

[a] Baseline case uses: rigid foundation, Corralitos Channels 1 (horizontal) and 2 (vertical) as input motions, and Calibration No. 1 for the constitutive model.

[b] Parameter h_{po} reduced to 30 to maintain the same cyclic strengths as the baseline case.

[c] Parameter h_{po} increased to 55 to maintain the same cyclic strengths as the baseline case.

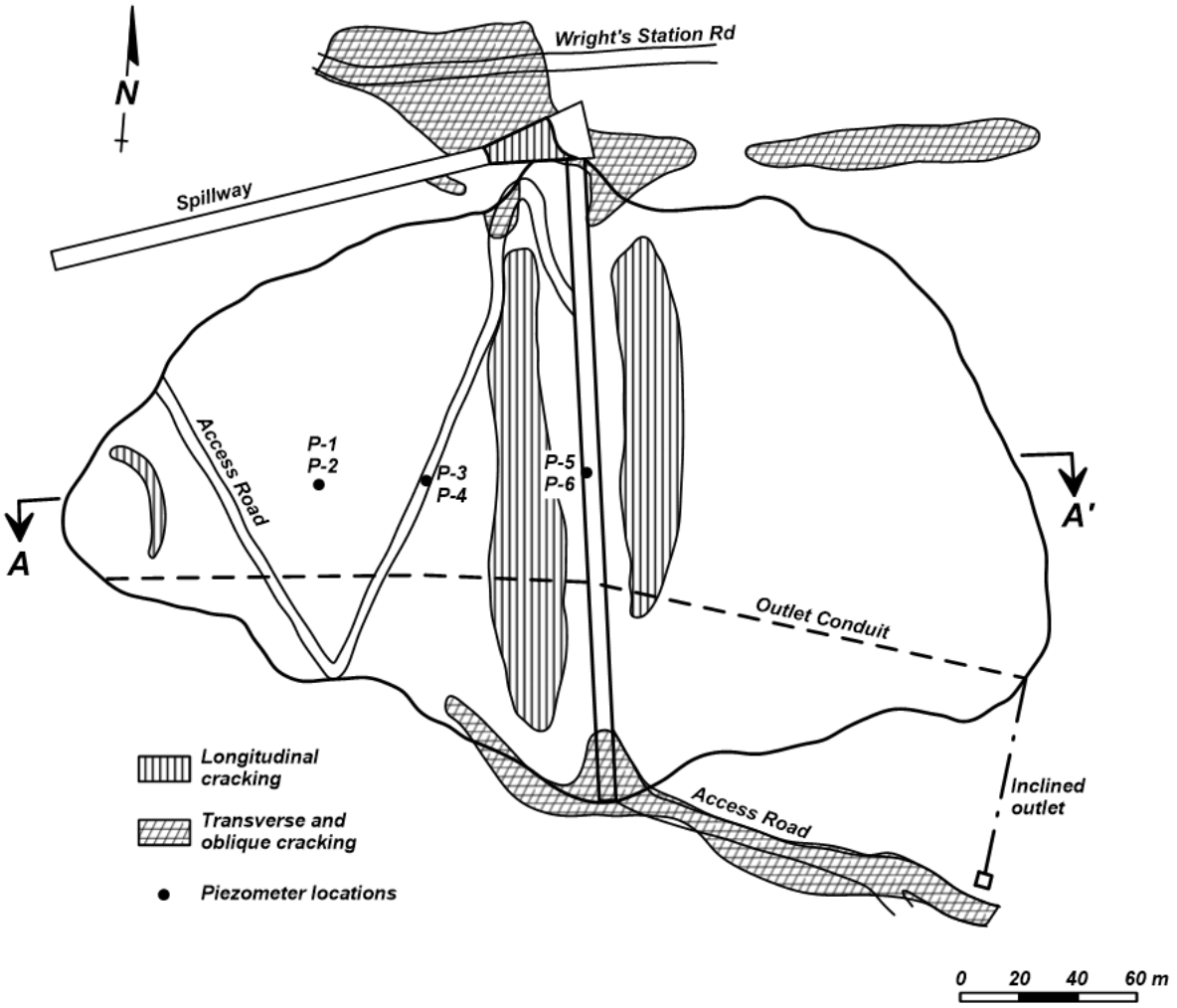

Figure 1. Plan view with areas of cracking induced by the 1989 Loma Prieta earthquake and locations of piezometers at that time (redrawn after Wahler Associates 1990 and Harder et al. 1998)

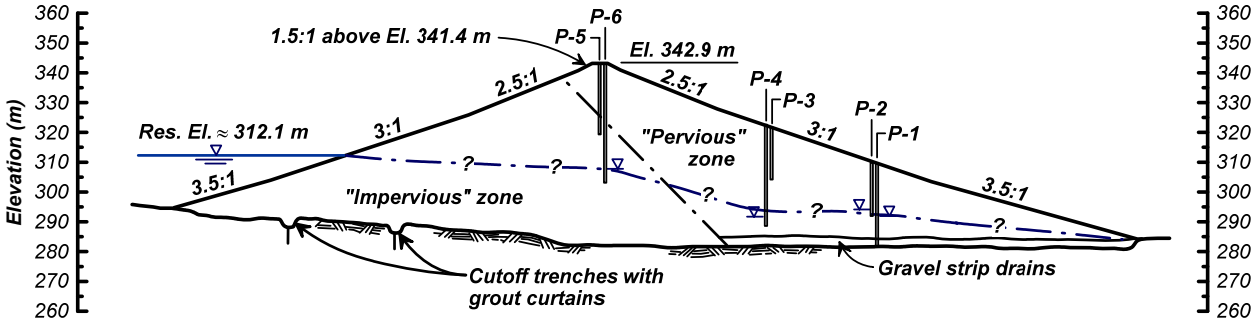

Figure 2. Maximum cross-section (A-A') showing phreatic surface based on piezometer records (redrawn after Wahler Associates 1990 and Harder et al. 1998)

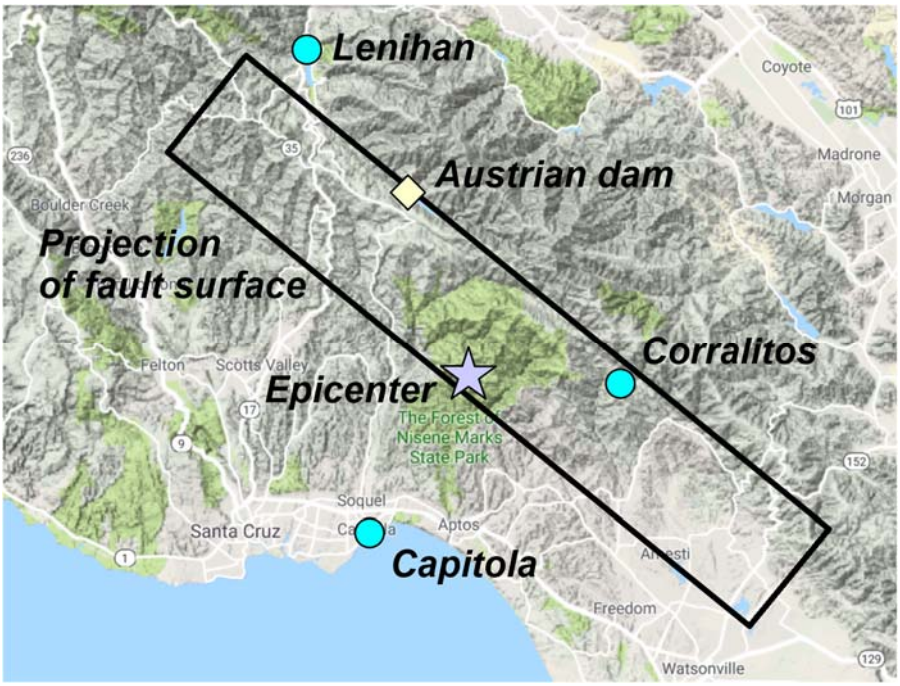

Figure 3. Location of Austrian Dam relative to the Corralitos and Lenihan recording stations and the vertical projection of the fault surface by Wald et al. (1991); base map from Google.

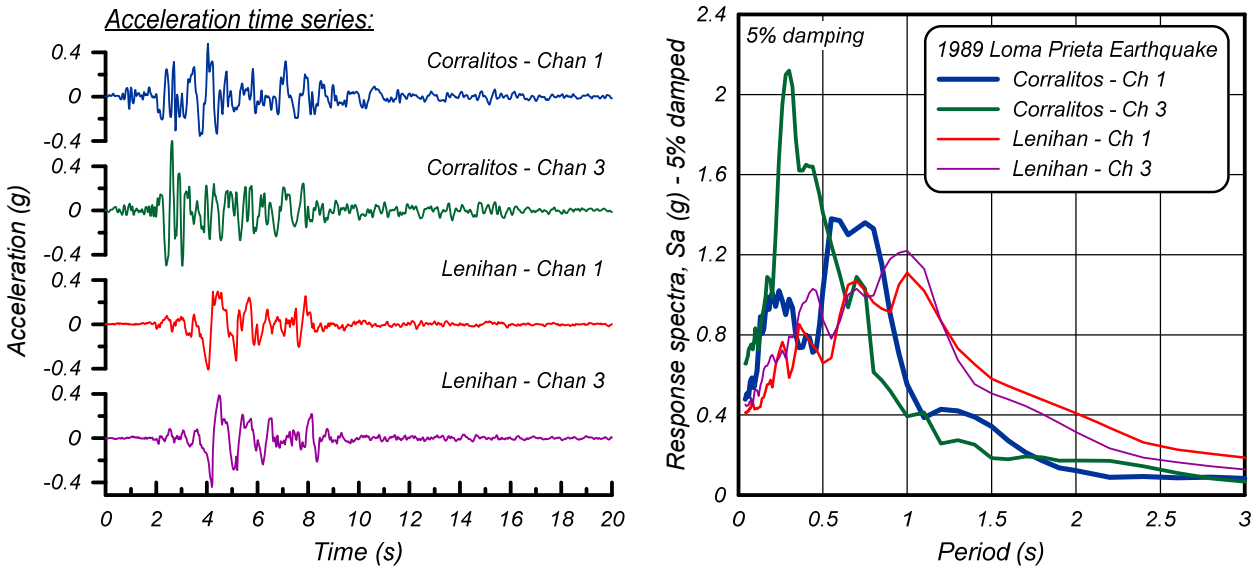

Figure 4. Horizontal acceleration time series and acceleration response spectra for the Corralitos station and Lenihan abutment station recordings

Figure 5. Photographs of cracking after Loma Prieta earthquake: (a) longitudinal and transverse cracking on the dam crest near the left abutment, (b) cracking along access road on the lower portion of the downstream face (California Division of Safety of Dams files 1989)

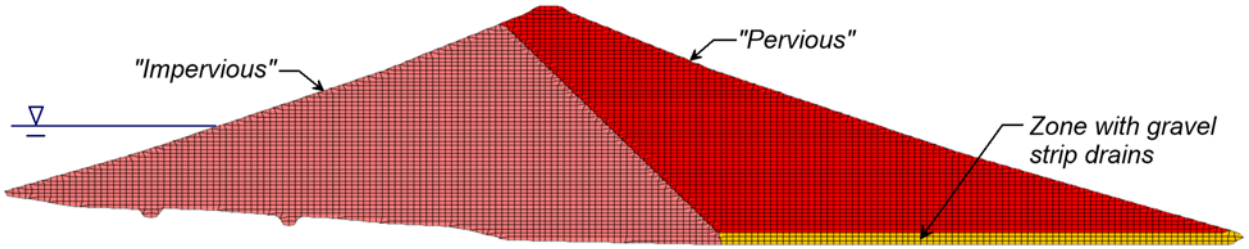

(a)

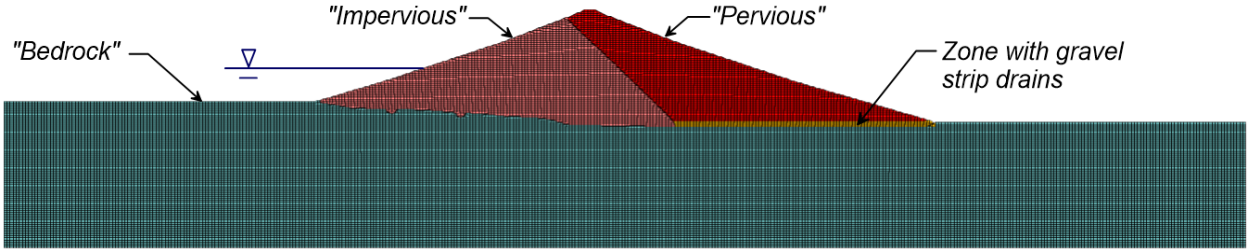

(b)

Figure 6. Mesh and zoning for the numerical model: (a) embankment mesh with a rigid foundation, and (b) same embankment mesh on a 60-m thick layer of bedrock

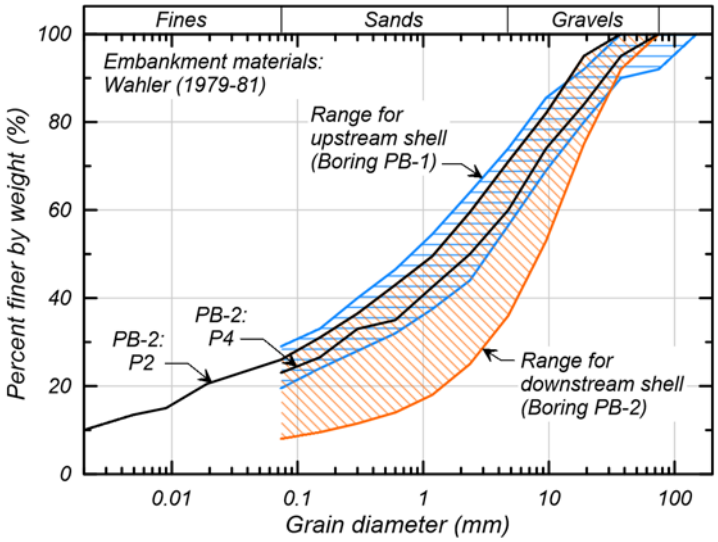

Figure 7. Grain size distribution ranges for samples from borings located on the upstream face (boring PB-1) and downstream face (boring PB-2), along with grain size distributions for the two ICU triaxial test specimens obtained from boring PB-2 (data from Wahler 1979, 1981)

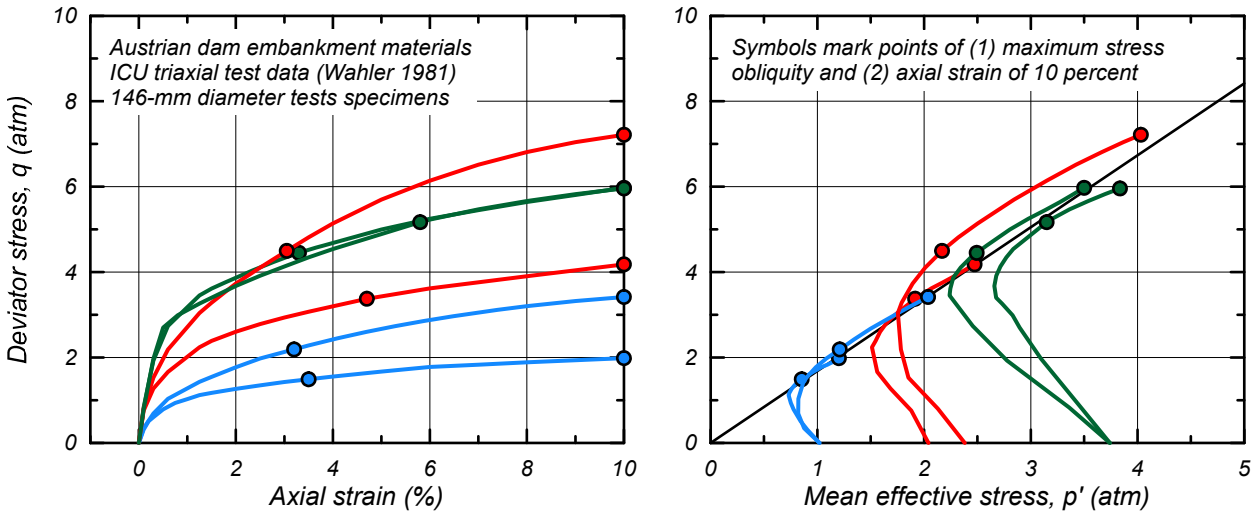

Figure 8. Results of ICU triaxial compression tests on tube samples obtained from both the upstream and downstream sides of the embankment (digitized from data presented in Wahler 1981)

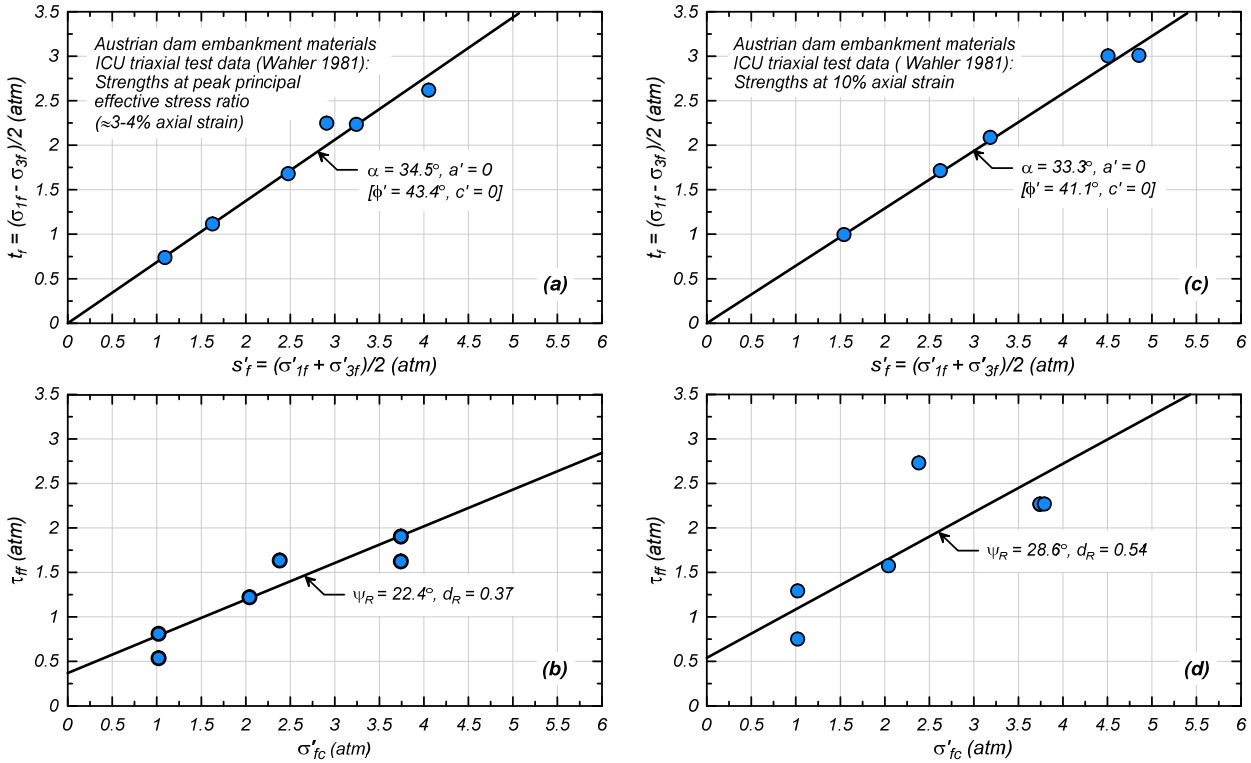

Figure 9. Results of ICU triaxial compression tests (data from Wahler Associates 1979): (a) effective stress strength parameters at peak principal effective stress ratio, (b) undrained shear strength at peak principal effective stress ratio, (c) effective stress strength parameters at 10% axial strain, and (d) undrained shear strength at 10% axial strain.

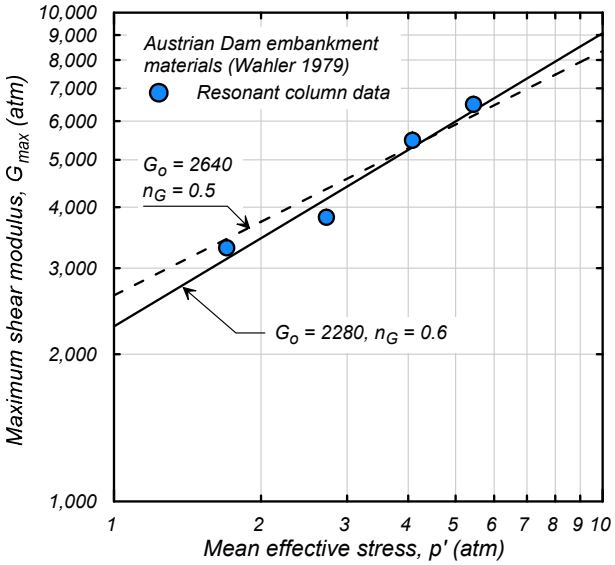

Figure 10. Maximum shear modulus data and alternative relationships for the embankment materials

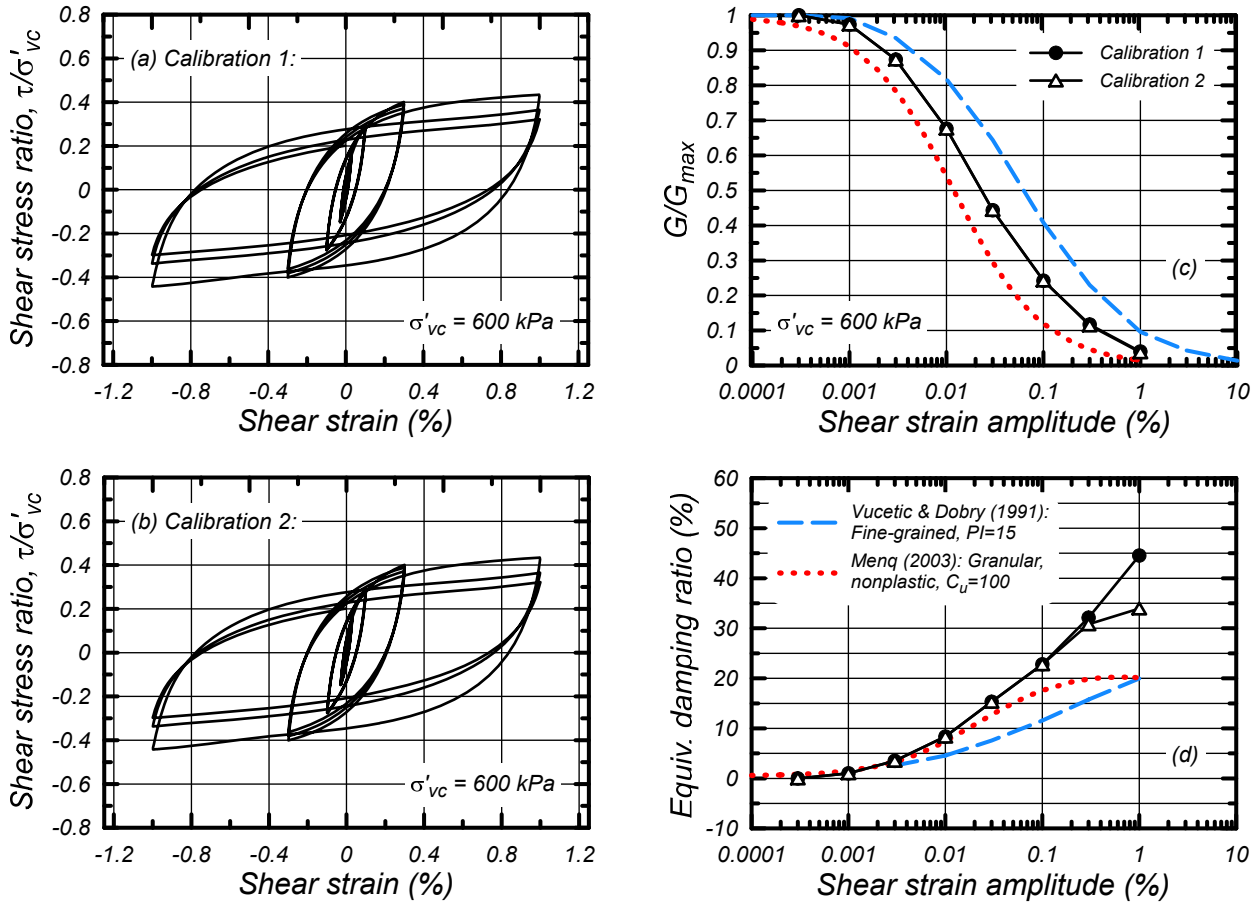

Figure 11. Cyclic undrained DSS loading at constant strain amplitudes: (a) stress-strain response for Calibration 1, (b) stress-strain response for Calibration 2, (c) shear modulus reduction versus shear strain amplitude, and (d) equivalent damping ratios versus shear strain amplitude.

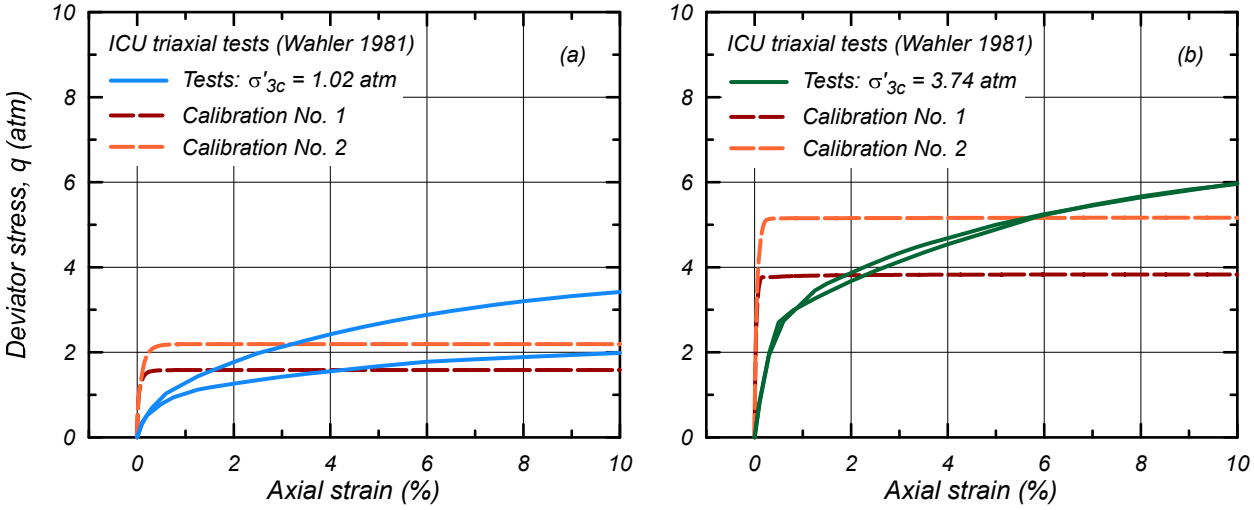

Figure 12. Simulations of monotonic undrained compression loading using PM4Silt (in plane-strain) and results ICU triaxial compression tests for consolidation stresses of: (a) 1.02 atm, and (b) 3.74 atm.

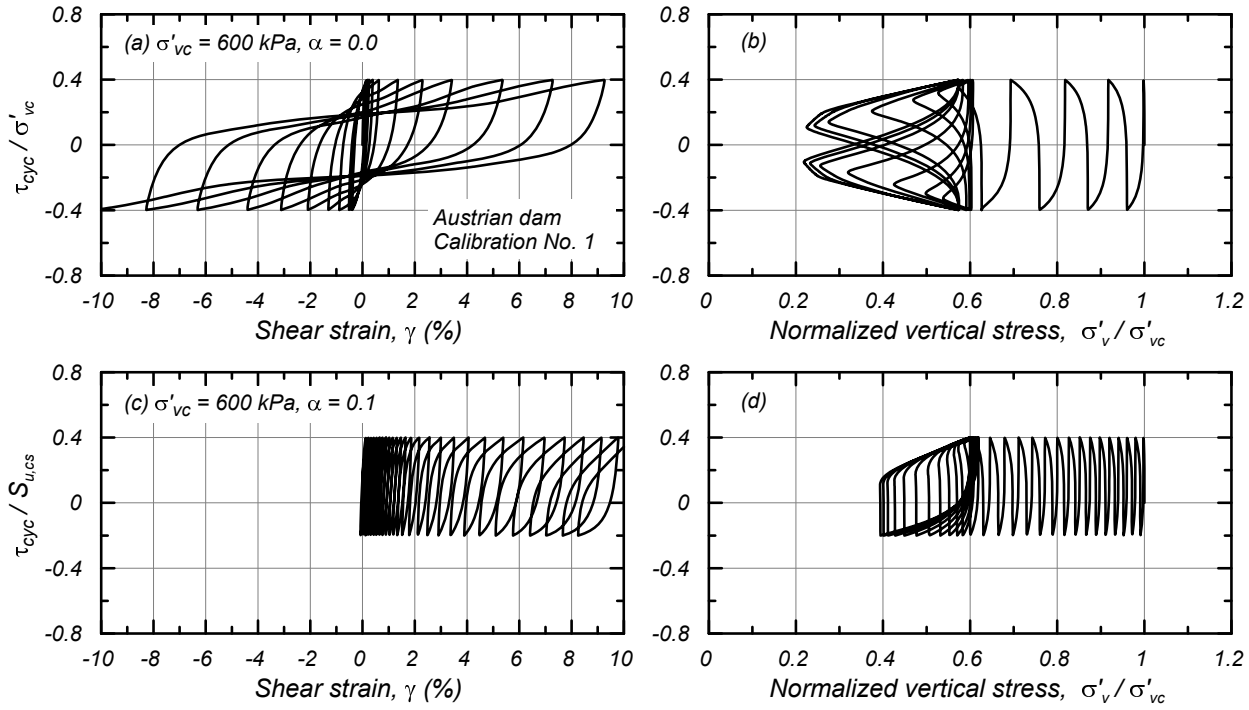

Figure 13. Stress-strain and stress path responses in cyclic undrained DSS loading for Calibration 1 with a vertical consolidation stress of 600 kPa: (a & b) initial static shear stress ratio of 0.0, and (c & d) initial static shear stress ratio of 0.1.

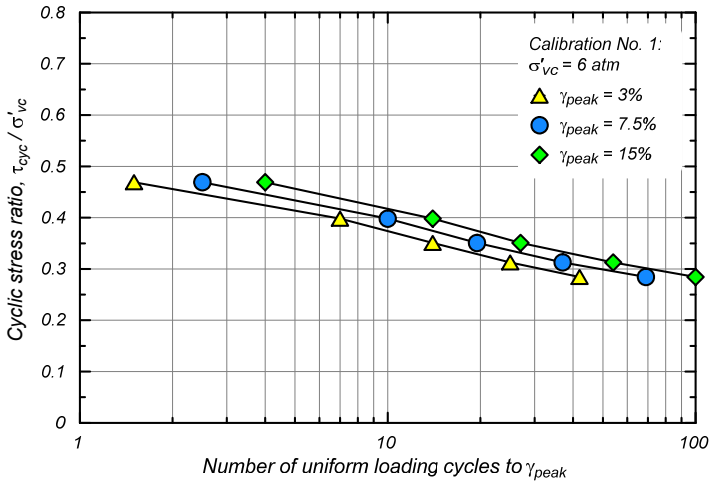

Figure 14. Cyclic stress ratio versus number of uniform loading cycles to different peak shear strains in cyclic undrained DSS loading for Calibration 1 with a vertical consolidation stress of 6 atm (608 kPa)

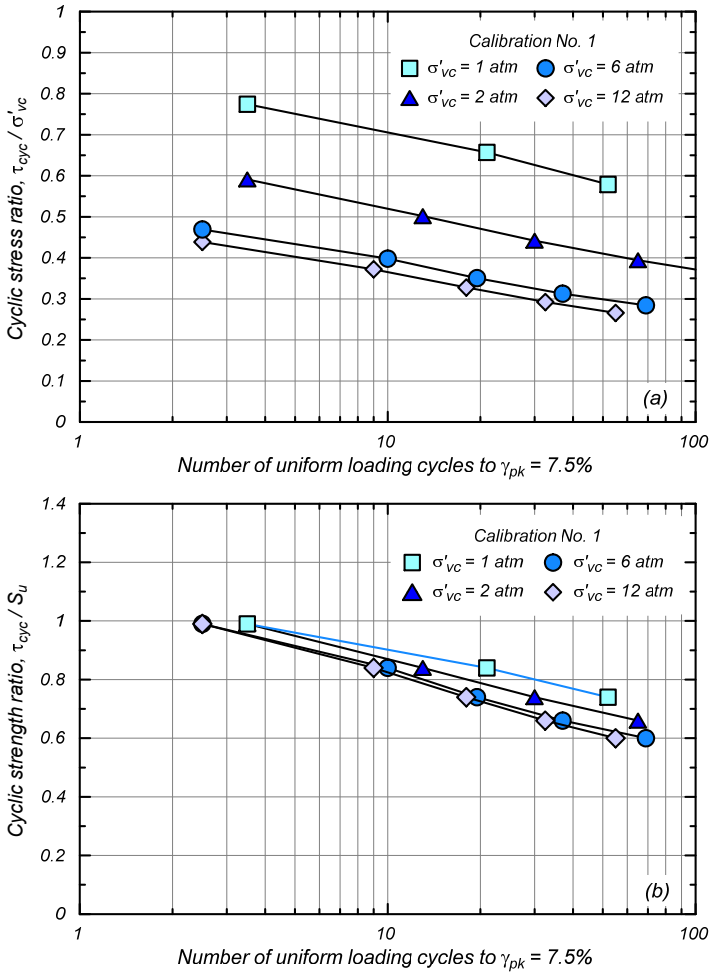

Figure 15. Cyclic strengths in cyclic undrained DSS loading for Calibration 1 with vertical consolidation stresses of 1 to 12 atm: (a) cyclic stress ratio, and (b) cyclic strength ratio.

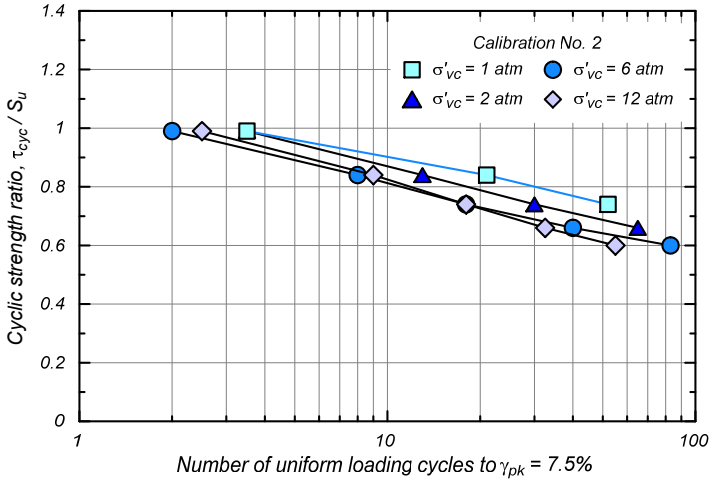

Figure 16. Cyclic strength ratios in cyclic undrained DSS loading for Calibration 2 with vertical consolidation stresses of 1 to 12 atm.

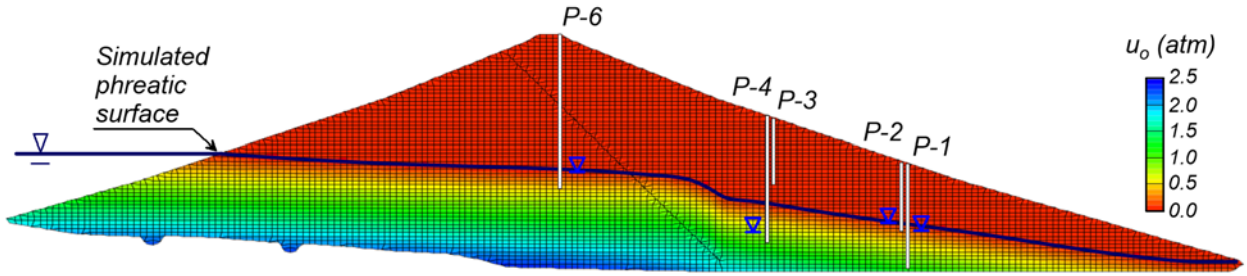

Figure 17. Comparison of seepage analysis results with pre-earthquake piezometer data

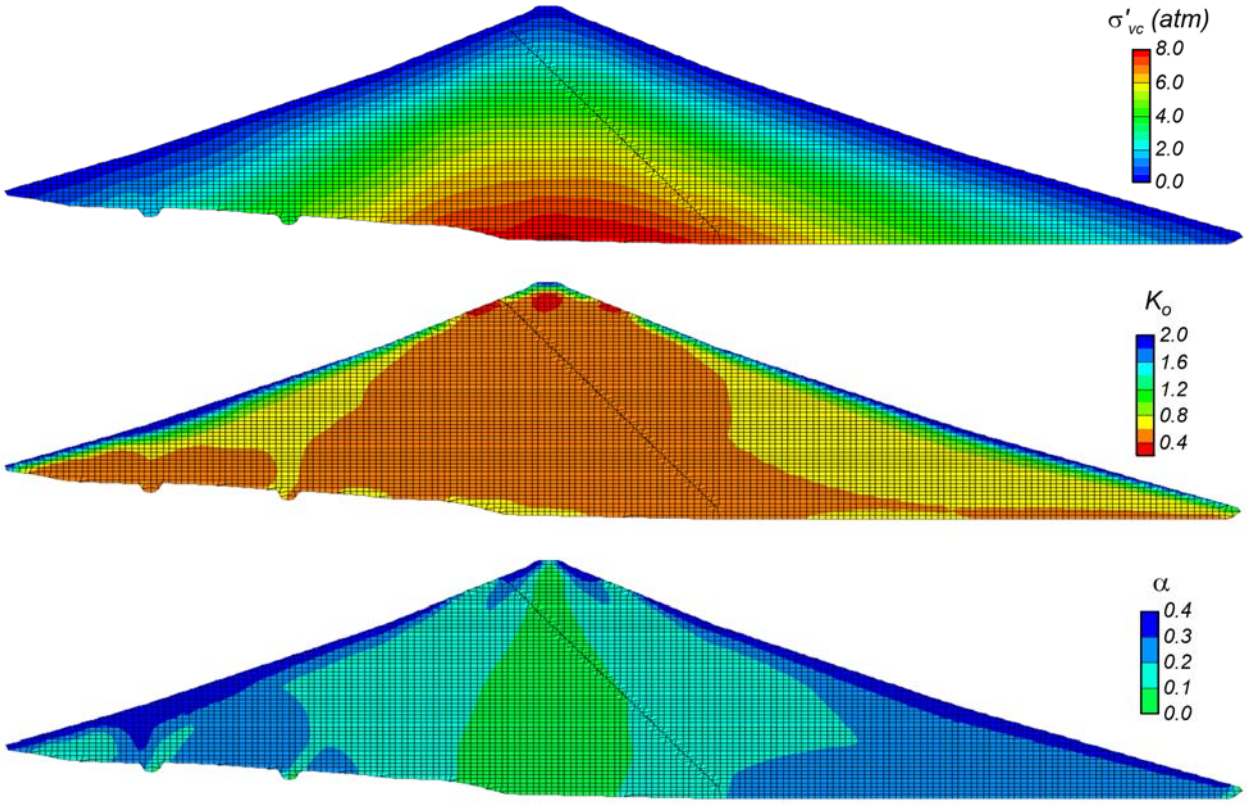

Figure 18. Initial static stress conditions: (a) vertical effective stress, σ'_v (b) coefficient of lateral earth pressure at rest, K_o, and (c) initial horizontal static shear stress ratio, α.

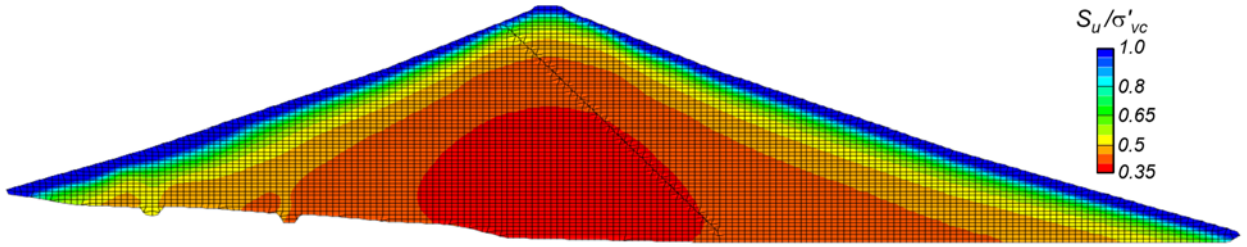

Figure 19. Contours of undrained shear strength as a ratio of vertical consolidation stress

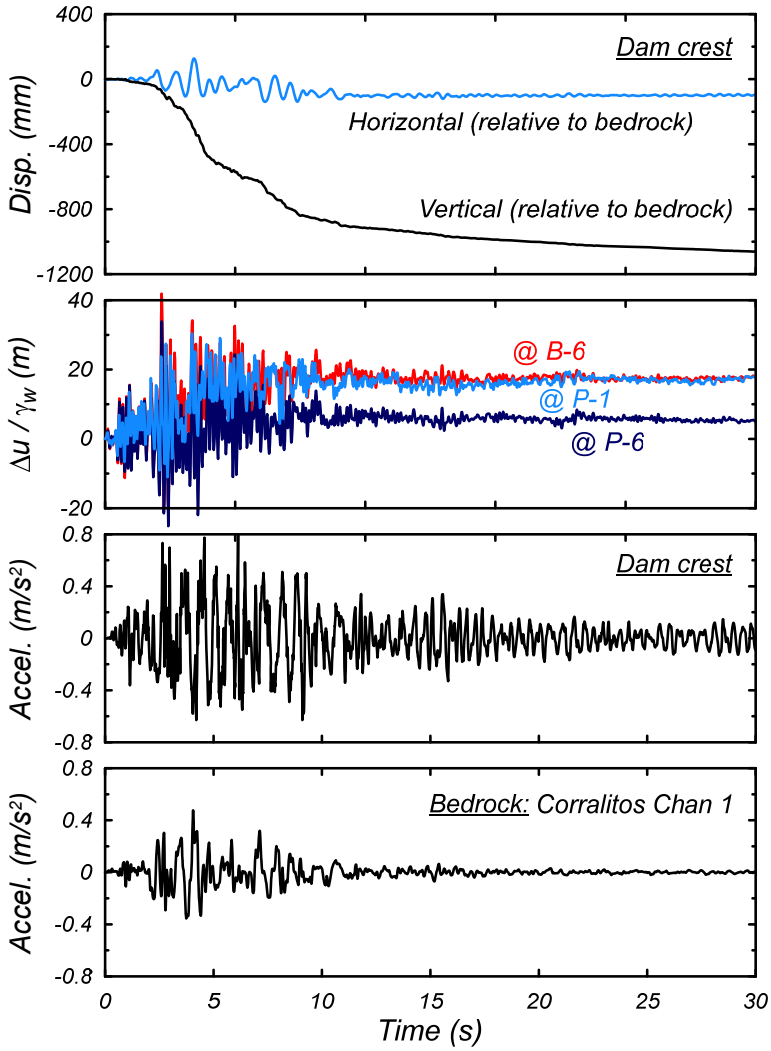

Figure 20. Time series of acceleration, displacement, and excess pore pressure computed for Calibration 1 with the Corralitos Channel 1 recording as the horizontal input motion

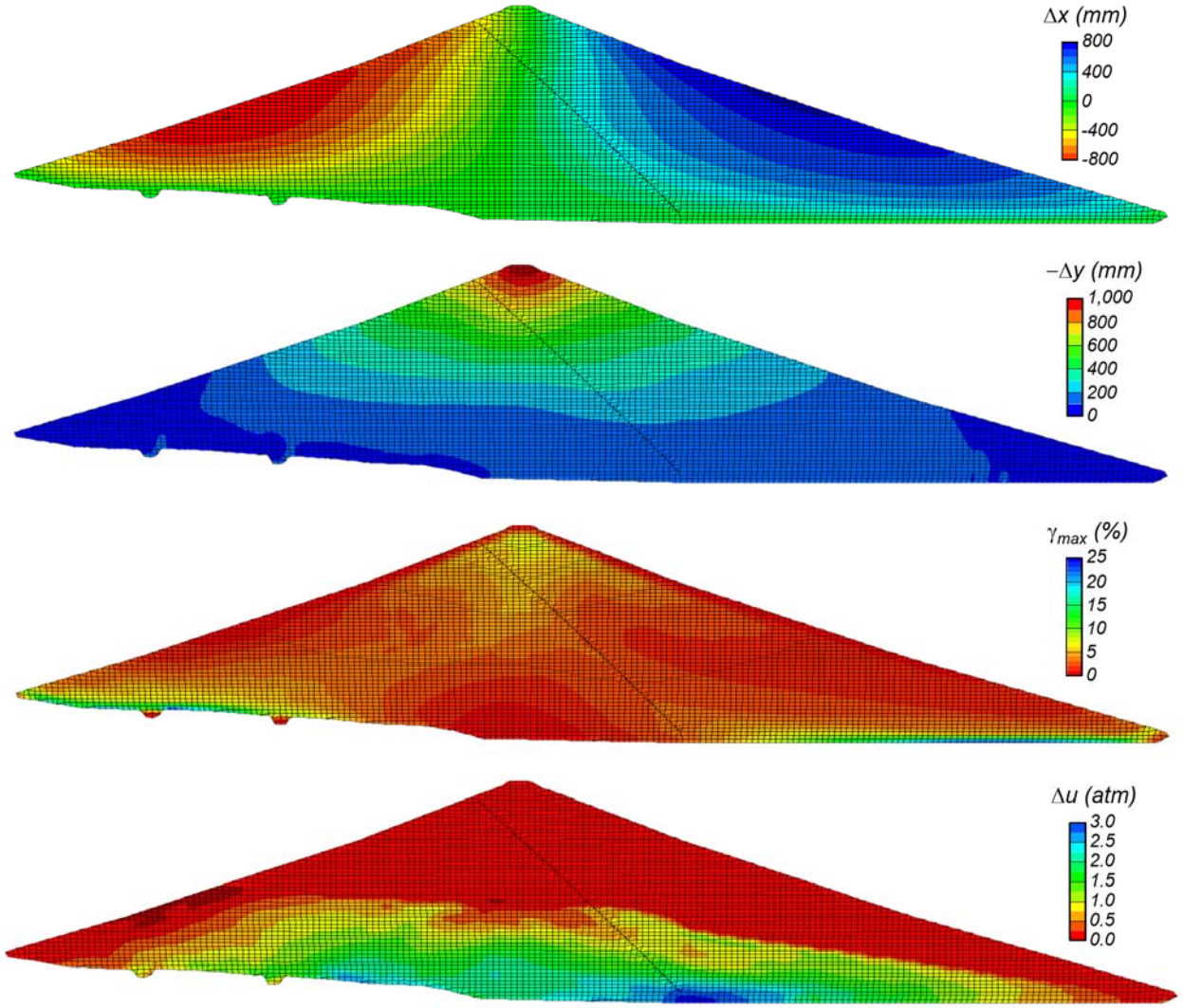

Figure 21. Deformations and pore pressures at the end of shaking for Calibration 1 with Corralitos Channel 1 as the horizontal input motion: (a) contours of horizontal displacement, (b) contours of vertical displacement, (c) contours of shear strain, and (d) contours of excess pore water pressure.

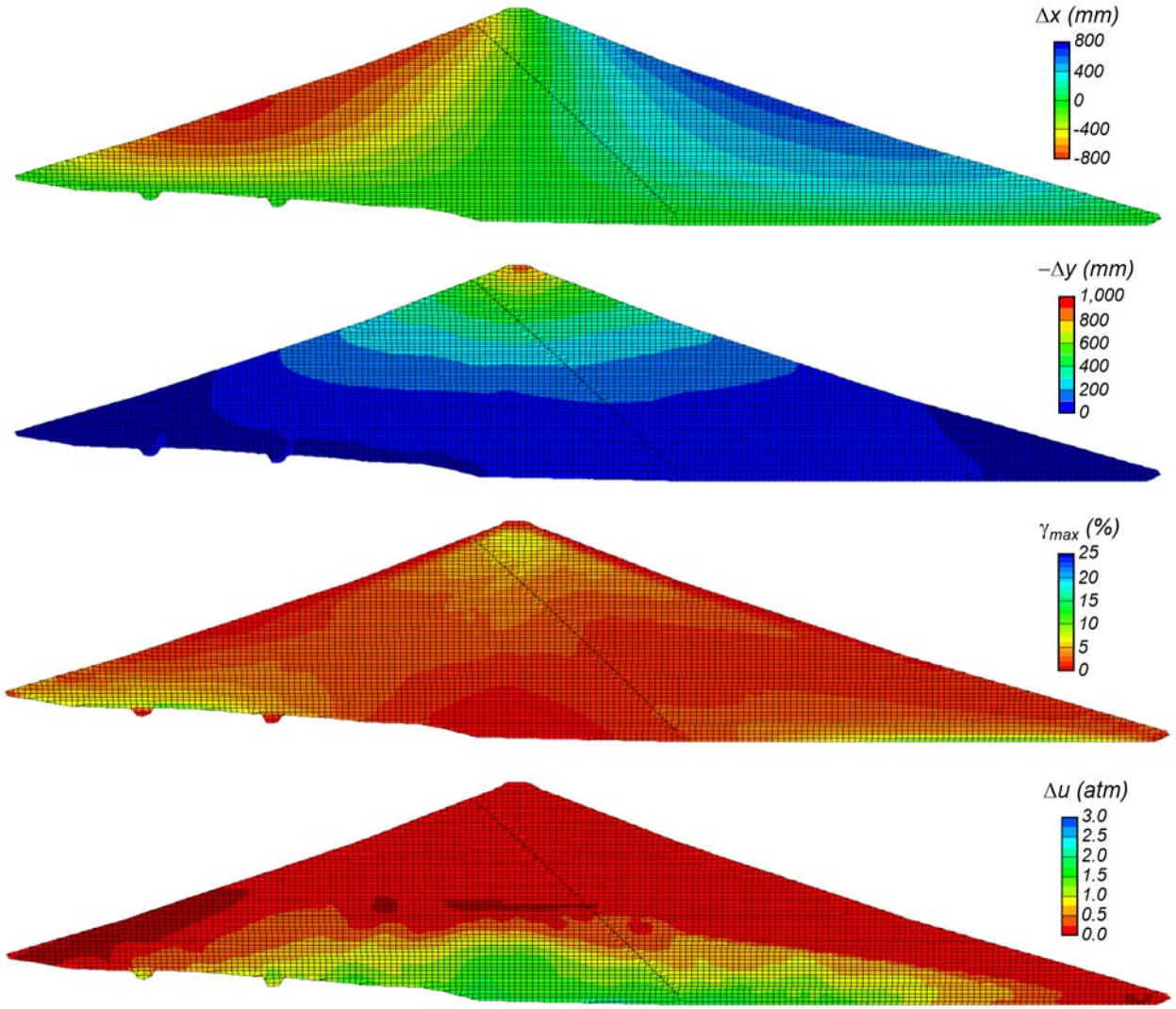

Figure 22. Deformations and pore pressures at the end of shaking for Calibration 2 with Corralitos Channel 1 as the horizontal input motion: (a) contours of horizontal displacement, (b) contours of vertical displacement, (c) contours of shear strain, and (d) contours of excess pore water pressure.